First results on nucleon resonance electroexcitation amplitudes from $ep \rightarrow e'\pi^+\pi^-p'$ cross sections at $W = 1.4$–1.7 GeV and $Q^2 = 2.0$–5.0 GeV^2

V. I. Mokeev [1,*], P. Achenbach [1], V. D. Burkert,[1] D. S. Carman [1], R. W. Gothe [2], A. N. Hiller Blin [3],
E. L. Isupov [4], K. Joo [5], K. Neupane [2] and A. Trivedi [2]

[1]*Thomas Jefferson National Accelerator Facility, Newport News, Virginia 23606, USA*
[2]*University of South Carolina, Columbia, South Carolina 29208, USA*
[3]*Institute for Theoretical Physics, Tübingen University, D-72076 Tübingen, Germany*
[4]*Skobeltsyn Institute of Nuclear Physics and Physics Department, Lomonosov Moscow State University, 119234 Moscow, Russia*
[5]*University of Connecticut, Storrs, Connecticut 06269, USA*

The electroexcitation amplitudes or $\gamma_v pN^*$ electrocouplings of the $N(1440)1/2^+$, $N(1520)3/2^-$, and $\Delta(1600)3/2^+$ resonances were obtained for the first time from the $ep \rightarrow e'\pi^+\pi^-p'$ differential cross sections measured with the CLAS detector at Jefferson Lab within the range of invariant mass $W = 1.4$–1.7 GeV of the final state hadrons, for photon virtualities $Q^2 = 2.0$–5.0 GeV^2. A good description of the nine independent onefold differential $\gamma_v p \rightarrow \pi^+\pi^-p'$ cross sections achieved within the data-driven Jefferson Lab-Moscow State University (JM) meson-baryon reaction model in each bin of (W, Q^2) allows for separation of the resonant and nonresonant contributions. The electrocouplings were determined in the fits of the $\pi^+\pi^-p$ cross sections within three overlapping W intervals with a substantial contribution from each of the three resonances listed above. Consistent results on the electrocouplings extracted from the data in these W intervals provide evidence for their reliable extraction. These studies extend information on the electrocouplings of the $N(1440)1/2^+$ and $N(1520)3/2^-$ available from this channel over a broader range of Q^2. The electrocouplings of the $\Delta(1600)3/2^+$, which decays preferentially into $\pi\pi N$ final states, have been determined for the first time. The reliable extraction of the electrocouplings for these states is also supported by the description of the $\pi^+\pi^-p$ differential cross sections with Q^2-independent masses and total/partial hadronic decay widths into the $\pi\Delta$ and ρp final states.

I. INTRODUCTION

Studies of exclusive $\pi^+\pi^-p$ photo- and electroproduction off protons represent an effective tool for the exploration of the spectrum and structure of nucleon resonances [1–5]. In this work we will use N^* to represent both excited nucleon states $N(\text{mass})J^P$, as well as Delta states $\Delta(\text{mass})J^P$. Measurements with the CLAS detector have provided the dominant part of the available world information on exclusive meson electroproduction in the resonance region for $W < 2$ GeV and $Q^2 < 5$ GeV^2 [1–3,6–8]. The $\pi^0 p$, $\pi^+ n$, and $\pi^+\pi^-p$ electroproduction channels account for the largest part of the inclusive virtual photon-proton cross sections in the resonance excitation region [1]. The data on πN and $\pi^+\pi^-p$ electroproduction offer complementary information on the nucleon resonance electroexcitation amplitudes, the so-called $\gamma_v pN^*$ electrocouplings, and their evolution with photon virtuality Q^2 ($Q^2 = -q_\mu^2$), where q_μ is the virtual photon four-momentum.

The low-lying N^* states in the mass range below 1.6 GeV decay preferentially into πN, making single-pion electroproduction data the driving source of information on the electrocouplings of these states [8–10]. On the other hand, the branching fraction (BF) of these resonance decays into $\pi\pi N$

remains appreciable at the level of around 40%, allowing for an independent determination of their electrocouplings from this channel [11,12]. Consistent results on the electrocouplings from independent studies of πN and $\pi^+\pi^-p$ demonstrate the capability of the $\pi^+\pi^-p$ reaction model to provide extraction of these quantities and to evaluate the systematic uncertainties associated with their determination [12,13].

Several N^*'s in the mass range above 1.6 GeV decay preferentially into the $\pi\pi N$ final states with BF around 70%, making studies of $\pi^+\pi^-p$ electroproduction the major source of information on the electrocouplings of these states [12]. At the same time, there are N^*'s with masses above 1.6 GeV that decay mostly to the πN final states [14]. Therefore, studies of both πN and $\pi^+\pi^-p$ electroproduction off protons are of particular importance to get information on the Q^2 evolution of the electrocouplings for most prominent nucleon resonances.

Coupled-channels approaches are making progress towards the extraction of the electrocouplings for low-lying N^* states from the combined analyses of meson photo-, electro-, and hadroproduction data. Recently, the πN and ηp electroproduction multipoles, which are directly related to the $\gamma_v pN^*$ electrocouplings, were determined from CLAS data within a multichannel analysis [15,16]. The first results on the electrocouplings of the $\Delta(1232)3/2^+$ and $N(1440)1/2^+$ at their pole positions in the complex energy plane have become

*mokeev@jlab.org

available from the global multichannel analysis developed by the Argonne-Osaka Collaboration [17]. The contributions from the $\pi\Delta$ and ρp channels deduced from the $\pi^+\pi^-p$ cross sections play an important role in the development of these approaches [12,18]. Experiments of the 6-GeV era with the CLAS detector [19] in Hall B at Jefferson Lab have provided the first and still only available information on the Q^2 evolution of the electrocouplings of most resonances in the mass range up to 1.8 GeV for $Q^2 < 5$ GeV^2 [1,2].

Studies of $\pi^+\pi^-p$ photo- and electroproduction also provide a promising avenue in the search for the so-called missing resonances. Constituent quark models based on approximate symmetries of the strong interaction that are relevant for the strongly coupled regime, when the QCD running coupling α_s/π is comparable to unity, predict many more N^*'s than have been seen in experiments with both electromagnetic and hadronic probes [20–23]. These expectations are supported by the results on the N^* spectrum obtained starting from the QCD Lagrangian within both lattice and continuum QCD approaches [24,25].

The combined analysis of the CLAS $\pi^+\pi^-p$ photo- and electroproduction data [26,27] carried out for $W = 1.6$–1.8 GeV and $Q^2 = 0$–1.5 GeV^2 revealed the presence of a new $N'(1720)3/2^+$ baryon state [4]. Only after implementation of this state with photo-/electrocouplings, mass, and decay widths fit to the CLAS data was a successful description of the $\pi^+\pi^-p$ photo-/electroproduction data achieved with Q^2-independent masses and decay widths into the $\pi\Delta$ and ρp final states. The contributions from the $N(1720)3/2^+$ and the new $N'(1720)3/2^+$ are well separated in the $\pi^+\pi^-p$ photo-/electroproduction data analyses despite their close masses and same spin-parity due to their different patterns for decay into intermediate $\pi\Delta$ and ρp states and the different Q^2 evolutions of their electrocouplings. These differences can only be seen in the combined studies of $\pi^+\pi^-p$ photo- and electroproduction, but they were elusive in previous studies of the two-body meson-baryon channels. Therefore, such combined studies provide a promising avenue in the quest to discover additional resonances.

The CLAS results on the electrocouplings make it possible for the first time to determine the resonant contributions to the inclusive electron scattering structure functions in the resonance region [28–30]. They also provide a new opportunity to better understand the ground state nucleon parton distribution functions (PDFs) at large values of the fractional parton momentum x within the resonance region.

Analyses of the CLAS results on the Q^2 evolution of the electrocouplings within coupled-channels approaches [17,31] and continuum Schwinger methods (CSMs) [32], supported by the results from different quark models [33–36], have revealed N^* structure as an interplay between the inner core of three dressed quarks and an external meson-baryon cloud [1,3,17,37]. Studies of the electrocouplings for $Q^2 \lesssim 2$ GeV^2 provide important information on the transition from confined dressed quarks to deconfined mesons and baryons that give rise to the meson-baryon cloud.

Analyses of these electrocouplings suggest a gradual transition from the convolution between the meson-baryon cloud and quark core in N^* structure towards quark core domi-

nance with increasing Q^2 [32,34–36]. Virtual photons with $Q^2 \gtrsim 1$–2 GeV^2 penetrate the meson-baryon cloud and interact mostly with the quark core. Consequently, studies of the electrocouplings in this higher Q^2 regime provide a unique way to explore the structure of dressed quarks and the evolution of their interactions at distance scales from the strongly coupled to the perturbative (pQCD) regimes [38–41]. Therefore, the region of high Q^2 looks promising to explore many facets of the strong interaction dynamics between three dressed quarks apparent in the generation of various N^*'s with different quantum numbers and structure.

The description of the $\Delta(1232)3/2^+$ and $N(1440)1/2^+$ electrocouplings achieved within CSMs [42,43] by employing the same momentum dependence of the dressed quark mass deduced from the QCD Lagrangian [39,41] and used in the description of the pion and nucleon elastic electromagnetic form factors [42,44,45] demonstrated the promising opportunity for gaining insight into the emergence of more than 98% of the hadron mass from data on the Q^2 evolution of the electrocouplings.

As of now, the electrocouplings are available from $\pi^+\pi^-p$ electroproduction cross sections within the range of $Q^2 < 1.5$ GeV^2. In this paper, we present an extension of the results on the electrocouplings of the $N(1440)1/2^+$ and $N(1520)3/2^-$ determined from the $\pi^+\pi^-p$ cross sections at $W = 1.4$–1.7 GeV for $Q^2 = 2.0$–5.0 GeV^2 and compare them with the available results from the studies of πN electroproduction within the same kinematic domain. The $\Delta(1600)3/2^+$ recently was elevated to a four-star PDG status [14]. This state decays preferentially into $\pi\pi N$. The electrocouplings of the $\Delta(1600)3/2^+$ have become available for the first time from the analysis of the $\pi^+\pi^-p$ electroproduction data presented here.

This paper is organized as follows. In Sec. II we present the kinematic variables for the description of $\pi^+\pi^-p$ electroproduction and the onefold differential cross sections measured with CLAS used for the extraction of the electrocouplings in the mass range below 1.7 GeV. Here, we also discuss the updates to the Jefferson Lab-Moscow State University (JM) reaction model relevant to the extraction of the electrocouplings for $Q^2 = 2.0$–5.0 GeV^2. The procedures developed for the evaluation of the electrocouplings from the cross section fits are presented in Sec. III. The results on the electrocouplings and partial decay widths to $\pi\Delta$ and ρp for the $N(1440)1/2^+$, $N(1520)3/2^-$, and $\Delta(1600)3/2^+$ are presented in Sec. IV, along with comparisons of the electrocouplings from the $\pi^+\pi^-p$ data with those previously available from the analyses of πN data. The impact of these results on the understanding of N^* structure is presented in Sec. V. We conclude and highlight the future prospects for resonance electrocoupling studies from exclusive meson electroproduction data in Sec. VI.

II. CROSS SECTIONS AND REACTION MODEL FOR ELECTROCOUPLINGS

In this section we describe the $\pi^+\pi^-p$ differential cross sections measured with CLAS for $W = 1.4$–1.7 GeV and $Q^2 = 2.0$–5.0 GeV^2 [46,47] that were used for the extraction
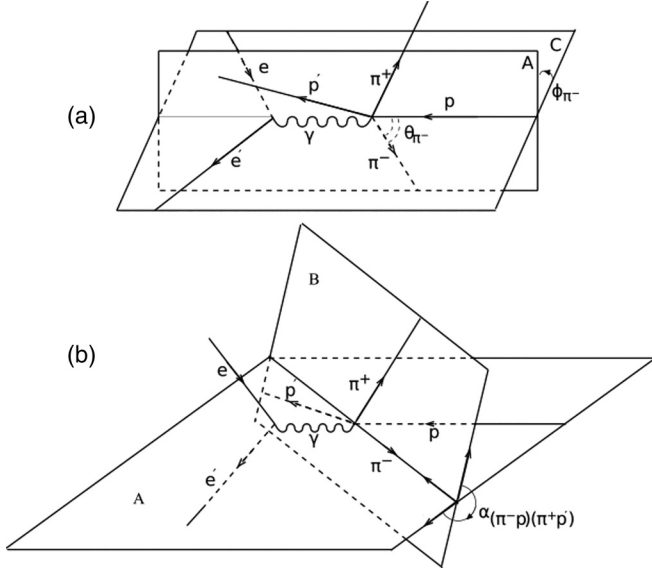
FIG. 1. Kinematic variables for the description of the reaction $\gamma_v p \rightarrow \pi^+ \pi^- p'$ in the CM frame of the final state hadrons corresponding to the $d^5\tau$ differential assignment given in Sec. II A. Panel (a) shows the π^- polar and azimuthal angles θ_{π^-} and ϕ_{π^-}. Plane C represents the electron scattering plane. The z axis is directed along the γ_v three-momentum, while the x axis is located in the electron scattering plane C and the y axis forms a right-handed coordinate system. Plane A is defined by the three-momenta of the initial state proton and the final state π^-. Panel (b) shows the angle $\alpha_{[\pi^- p][\pi^+ p']}$ between the two hadronic planes A and B or the plane B rotation angle around the axis aligned along the three-momentum of the final state π^-. Plane B is defined by the three-momenta of the final state π^+ and p'.

of the $N(1440)1/2^+$, $N(1520)3/2^-$, and $\Delta(1600)3/2^+$ parameters. We also present the basic features of the JM model relevant for the extraction of the electrocouplings from the $\pi^+\pi^- p$ data and the most recent JM model updates.

A. Kinematic variables and $\pi^+\pi^- p$ electroproduction cross sections

For the $\gamma_v p \rightarrow \pi^+ \pi^- p'$ reaction, the invariant mass of the final state hadrons W and photon virtuality Q^2 unambiguously determine the initial state virtual photon and proton four-momenta in their center-of-mass (CM) frame with the z axis directed along the γ_v three-momentum as shown in Fig. 1. The final $\pi^+\pi^- p$ state is described by the four-momenta of the three final state hadrons by 12 variables. Energy-momentum conservation reduces the number of variables down to 8. Since the three final state hadrons are on-shell, three additional relations between the final state hadron energies and absolute momentum values reduce the number of independent variables down to 5. Hence, at a given W and Q^2, the reaction can be fully described by the fivefold differential cross section $d^5\sigma/d^5\tau$, where $d^5\tau$ is differential in the five independent variables that determine the final state hadron four-momenta. There are many choices for these five variables [48]. After defining $M_{\pi^+ p}$, $M_{\pi^- p}$, and $M_{\pi^+\pi^-}$ as the invariant masses of the three possible two-hadron pairs in

TABLE I. Kinematic area covered in the fit of the CLAS $\pi^+\pi^- p$ electroproduction cross sections for the extraction of the resonance parameters [46,47].

	2.0–2.4
	2.2 for computed cross sections
	2.4–3.0
	2.6 for computed cross sections
Q^2 interval (GeV^2)	3.0–3.5
	3.2 for computed cross sections
	3.5–4.2
	3.6 for computed cross sections
	4.2–5.0
	4.4 for computed cross sections
W interval (GeV)	1.41–1.66
covered in each Q^2 bin	11 bins

the final state, we adopt here the following assignment for the computation of the fivefold differential cross section: $d^5\tau = dM_{\pi^+ p} dM_{\pi^+\pi^-} d\Omega_{\pi^-} d\alpha_{[\pi^- p][\pi^+ p']}$, where Ω_{π^-} is the final state π^- solid angle defined by the polar (θ_{π^-}) and azimuthal (ϕ_{π^-}) angles shown in Fig. 1(a), and $\alpha_{[\pi^- p][\pi^+ p']}$ is the rotation angle of plane B defined by the momenta of the final state π^+ and p' around the axis defined by the final state π^- momentum; see Fig. 1(b). This $d^5\tau$ differential is used in the computation of the $\pi^+\pi^- p$ cross sections within the JM model for comparison with the experimental data [49,50]. All frame-dependent variables are defined in the final state hadron CM frame.

The $\pi^+\pi^- p$ electroproduction data have been collected in the bins of a seven-dimensional space, since for the description of the initial state kinematics, W and Q^2 are required. The number of bins in the seven-dimensional reaction phase space and the kinematic area covered by the data for extraction of the differential cross sections are detailed in Tables I and II. The huge number of seven-dimensional bins over the reaction phase space ($\approx 1 \times 10^7$ bins) does not allow us to use the correlated multifold differential cross sections in the analysis of

TABLE II. List of the onefold differential cross sections measured with CLAS [46,47] and the binning over the kinematic variables. $M_{i,j} = M_i + M_j$ and $M_{i,j}^{\max} = W - M_k$, where $M_{i,j}$ and M_k are the invariant masses of the final state hadron pair (i, j) and the mass of the third final state hadron k, respectively.

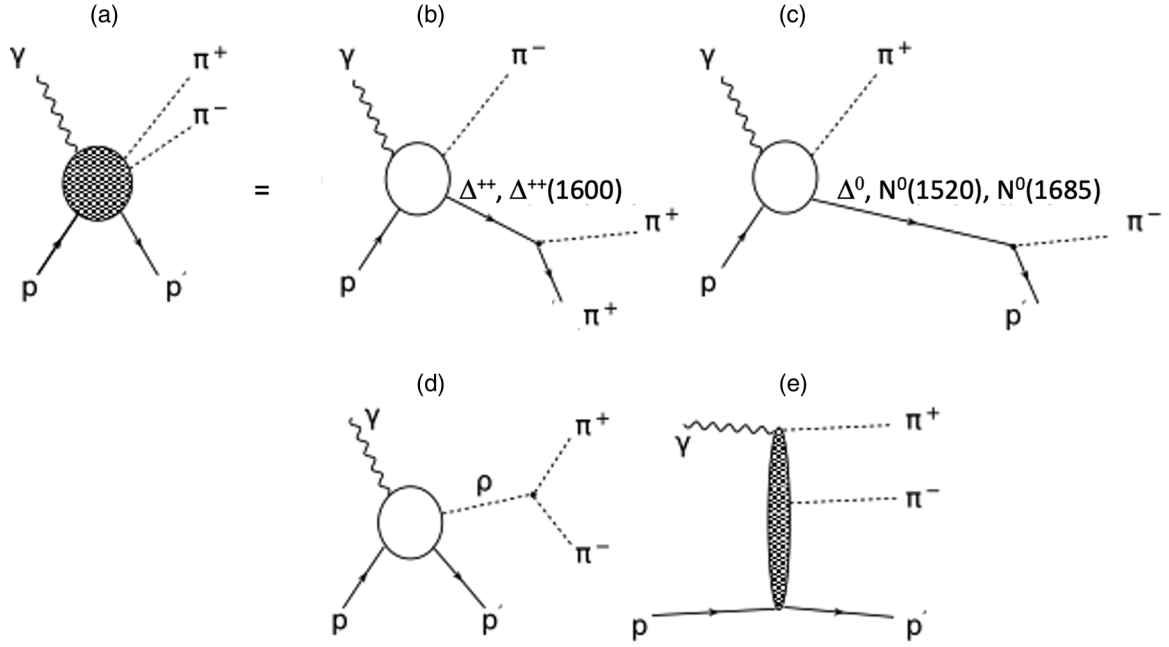| Onefold differential cross section	Interval covered	Number of bins
$\frac{d\sigma}{dM_{\pi^+ p}}$ (μb/GeV)	$M_{\pi^+ p}^{\min} - M_{\pi^+ p}^{\max}$	14
$\frac{d\sigma}{dM_{\pi^+\pi^-}}$ (μb/GeV)	$M_{\pi^+\pi^-}^{\min} - M_{\pi^+\pi^-}^{\max}$	14
$\frac{d\sigma}{dM_{\pi^- p}}$ (μb/GeV)	$M_{\pi^- p}^{\min} - M_{\pi^- p}^{\max}$	14
$\frac{d\sigma}{\sin\theta_{\pi^-} d\theta_{\pi^-}}$ (μb/rad)	0–180°	10
$\frac{d\sigma}{\sin\theta_{\pi^+} d\theta_{\pi^+}}$ (μb/rad)	0–180°	10
$\frac{d\sigma}{\sin\theta_{p'} d\theta_{p'}}$ (μb/rad)	0–180°	10
$d\sigma/d\alpha_{[\pi^- p][\pi^+ p']}$ (μb/rad)	0–360°	10
$d\sigma/d\alpha_{[\pi^+ p][\pi^- p']}$ (μb/rad)	0–360°	10
$d\sigma/d\alpha_{[\pi^+\pi^-][pp']}$ (μb/rad)	0–360°	10

FIG. 2. The $\gamma_v p \to \pi^+\pi^- p'$ electroproduction mechanisms incorporated at the amplitude level into the JM17 model [11,12,18]: (a) full amplitude; (b) $\pi^-\Delta^{++}$ and $\pi^-\Delta^{++}(1600)3/2^+$ subchannels; (c) $\pi^+\Delta^0$, $\pi^+N^0(1520)3/2^-$, and $\pi^+N^0(1680)5/2^+$ subchannels; (d) ρp subchannel; (e) direct 2π mechanisms.

the data. More than half of the five-dimensional phase-space bins of the final state hadrons at any given W and Q^2 remain unpopulated due to statistical limitations. Therefore, we use the following onefold differential cross sections in each bin of W and Q^2 covered by the data:

  (i) invariant mass distributions for the three pairs of the final state particles $d\sigma/dM_{\pi^+\pi^-}$, $d\sigma/dM_{\pi^+p}$, and $d\sigma/dM_{\pi^-p}$;

 (ii) distributions for the CM polar angles of the three final state particles $d\sigma/(\sin\theta_{\pi^-}d\theta_{\pi^-})$, $d\sigma/(\sin\theta_{\pi^+}d\theta_{\pi^+})$, and $d\sigma/(\sin\theta_{p'}d\theta_{p'})$;

(iii) distributions for the three α angles determined in the CM frame: $d\sigma/d\alpha_{[\pi^-p][\pi^+p']}$, $d\sigma/d\alpha_{[\pi^+p][\pi^-p']}$, and $d\sigma/d\alpha_{[\pi^+\pi^-][pp']}$, where $d\sigma/d\alpha_{[\pi^+p][\pi^-p']}$ and $d\sigma/d\alpha_{[\pi^+\pi^-][pp']}$ are defined analogously to $d\sigma/d\alpha_{[\pi^-p][\pi^+p']}$ described above.

The onefold differential cross sections were obtained by integrating the fivefold differential cross sections over the other four kinematic variables of $d^5\tau$. However, the angular distributions for the polar angles of the final state π^+ and p, as well as for the rotation angles around the axes along the momenta of these final state hadrons, cannot be obtained from $d^5\tau$ described above, since this differential does not depend on these variables. Two other sets of differentials $d^5\tau'$ and $d^5\tau''$ are required, which contain $d\Omega_{\pi^+}d\alpha_{[\pi^+p][\pi^-p']}$ and $d\Omega_{p'}d\alpha_{[pp'][\pi^+\pi^-]}$, respectively, as described in Refs. [11,50]. The fivefold differential cross sections evaluated over the other two differentials were computed from the fivefold differential cross section over the $d^5\tau$ differential by means of cross section interpolation. For each kinematic point in the five-dimensional phase space determined by the variables of the $d^5\tau'$ and $d^5\tau''$ differentials, the four-momentum of the

three final state hadrons were computed, and from these values, the five variables of the $d^5\tau$ differential were determined. The $d^5\sigma/d^5\tau$ cross sections were interpolated into this five-dimensional kinematic point.

B. Reaction model for extraction of electrocouplings

The $N(1440)1/2^+$, $N(1520)3/2^-$, and $\Delta(1600)3/2^+$ electrocouplings have been extracted for $Q^2 = 2.0\text{–}5.0$ GeV^2 from the data on the $\pi^+\pi^- p$ differential cross sections by fitting them within the framework of the data-driven JM reaction model detailed in Refs. [11,12,18], referred to as JM17, which was used for the extraction of the electrocouplings for $Q^2 < 1.5$ GeV^2 and $W < 1.8$ GeV. Within this approach, the $\pi^+\pi^- p$ electroproduction mechanisms seen through their manifestation in the observables as peaks in the invariant mass distributions for the final state hadrons and with pronounced dependencies in the CM angular distributions for the final state hadrons were incorporated. The remaining mechanisms without pronounced kinematic dependencies were accounted for by exploring the correlations between the shapes of their contributions into the nine independent onefold differential cross sections.

The mechanisms incorporated into the JM model are shown in Fig. 2. The amplitudes of the $\gamma_v p \to \pi^+\pi^- p'$ reaction are described as a superposition of the $\pi^-\Delta^{++}$, $\pi^+\Delta^0$, ρp, $\pi^+N^0(1520)$, and $\pi^+N^0(1680)$ subchannels with subsequent decays of the unstable hadrons to the final state $\pi^+\pi^- p$ state as detailed in Appendix III of Ref. [18]. In addition, direct 2π production mechanisms, where the final $\pi^+\pi^- p$ comes about without going through the intermediate process of forming unstable hadron states are included. Evidence for these contributions is seen in analyses of the final state hadron

TABLE III. List of resonances included in the fit of the $\pi^+\pi^-p$ differential cross sections within the JM23 model and their parameters: Masses, total decay widths Γ_{tot}, and ranges of their variation. The JM17 model contains all listed resonances, except for the $\Delta(1600)3/2^+$. The starting values for the resonance electrocouplings were taken from the references given in the last column. The electrocouplings of the $N(1650)1/2^-$, $N(1720)3/2^+$, $N'(1720)3/2^+$, and $\Delta(1620)1/2^-$ were obtained for $Q^2 < 1.5$ GeV^2 and extrapolated to the Q^2 area covered by the CLAS data [46,47] as described in Ref. [30]. The predictions of Ref. [51] were used as the starting values for the $\Delta(1600)3/2^+$ electrocouplings.

N^* state incorporated in data fit	Mass (GeV)	Total decay width Γ_{tot} (GeV)	Ref.
$N(1440)1/2^+$	1.43–1.48	0.25–0.40	[10]
$N(1520)3/2^-$	1.51–1.53	0.12–0.13	[10]
$N(1535)1/2^-$	1.51–1.55	0.12–0.18	[10]
$N(1650)1/2^-$	1.64–1.67	0.15–0.16	[30]
$N(1680)5/2^+$	1.68–1.69	0.11–0.13	[9]
$N(1700)3/2^-$	1.65–1.75	0.16–0.18	[9]
$N'(1720)3/2^+$	1.71–1.74	0.11–0.13	[4]
$N(1720)3/2^+$	1.73–1.76	0.11–0.13	[30]
$\Delta(1600)3/2^+$	1.50–1.64	0.20–0.30	[51]
$\Delta(1620)1/2^-$	1.60–1.66	0.11–0.15	[30]
$\Delta(1700)3/2^-$	1.67–1.73	0.23–0.32	[30]

angular distributions with the phenomenological amplitudes described in Ref. [18].

Within the JM17 model, only the $\pi^-\Delta^{++}$, $\pi^+\Delta^0$, and ρp channels contain contributions from N^*'s excited in the s channel for the $\gamma_v p$ interaction. The JM17 model incorporates contributions from all well-established N^* states listed in Table III, except for the $\Delta(1600)3/2^+$ that was not included. Note that the four-star $N(1675)5/2^-$ and $N(1710)1/2^+$ states were not included. The amplitudes for electroexcitation of the $N(1675)5/2^-$ off protons are suppressed in comparison with the electrocouplings of other resonances in the third resonance region. Furthermore, in this work we have only determined the $\gamma_v pN^*$ electrocouplings for resonances in the mass range below 1.6 GeV. In this case, only the tail from the weakly excited $N(1675)5/2^-$ can contribute. As well, studies of $\pi^+\pi^-p$ electroproduction in the third resonance region have revealed no evidence for contributions from the $N(1710)1/2^+$[4,26].

The resonant amplitudes are described by a unitarized Breit-Wigner ansatz [11], which accounts for the transition between the same and different resonances in the dressed resonance propagator, which makes the resonant amplitudes consistent with restrictions imposed by a general unitarity condition [52,53]. Quantum number conservation in the strong interaction allows for transitions between the pairs of N^* states, $N(1520)3/2^- \leftrightarrow N(1700)3/2^-$, $N(1535)1/2^- \leftrightarrow N(1650)1/2^-$, and $N(1720)3/2^+ \leftrightarrow N'(1720)3/2^+$, which are incorporated into the JM17 model.

The nonresonant amplitudes in the $\pi\Delta$ subchannels are described by the minimal set of current conserving Reggeized Born terms detailed in Ref. [18]. They include the contact, Reggeized t-channel π-in-flight, s-channel nucleon, and u-channel Δ-in-flight terms. Note, as W is going to threshold, the Reggeized t-channel term gradually transforms into the π-pole term, allowing use of the Reggeized Born terms at low W.

The $\pi^+N^0(1520)3/2^-$ and $\pi^+N^0(1680)5/2^+$ channels are described in the JM17 model by nonresonant contributions only. The amplitudes of the $\pi^+N^0(1520)3/2^-$ subchannel were derived from the nonresonant Born terms in the $\pi\Delta$ subchannels by implementing an additional γ_5 matrix that accounts for the opposite parities of the $\Delta(1232)3/2^+$ and $N(1520)3/2^-$ [18]. The magnitudes of the $\pi^+N^0(1520)3/2^-$ production amplitudes were independently fit to the data for each bin in W and Q^2. The contributions from the $\pi^+N^0(1520)3/2^-$ subchannel should be taken into account for $W > 1.5$ GeV. The $\pi^+N^0(1680)5/2^+$ contributions are seen in the data at $W > 1.6$ GeV. These contributions are almost negligible at smaller W. Effective t-channel exchange terms were employed in the JM17 model for parametrization of the amplitudes of this subchannel [18]. The magnitudes of the $\pi^+N^0(1680)5/2^+$ amplitudes were fit to the data for each bin in W and Q^2.

In general, unitarity requires the presence of direct 2π production mechanisms in the $\pi^+\pi^-p$ electroproduction amplitudes, where the final state is created without going through the intermediate step of forming unstable hadron states [54,55]. These 2π processes are beyond the aforementioned contributions from the two-body sub-channels and are implemented into the JM17 model. These mechanisms are incorporated by a sequence of two exchanges in the t and/or u channel by unspecified particles that belong to two Regge trajectories. The amplitudes of the 2π mechanisms are parametrized by a Lorentz-invariant contraction between the spin tensors of the initial and final state particles, while two exponential propagators describe the exchanges by unspecified particles. All details on the parametrization of the 2π mechanisms are available in Refs. [12,18]. The magnitudes of these amplitudes are fit to the data for each bin in W and Q^2.

The studies of the final state hadron angular distributions over α_i ($i = [\pi^-p][\pi^+p']$, $[\pi^+p][\pi^-p']$, $[\pi^+\pi^-][pp']$) in Ref. [12] demonstrated the need to implement relative phases for all 2π direct mechanisms included in the JM17 model determined in the data fit. The contributions from these mechanisms are maximal and substantial ($\approx$30%) for $W < 1.5$ GeV and they decrease with increasing W, contributing less than 10% for $W > 1.6$ GeV. However, even in this kinematic regime, these mechanisms can be seen in the $\pi^+\pi^-p$ cross sections due to an interference of the amplitudes with the two-body subchannels.

Representative examples of the description of the $\pi^+\pi^-p$ cross sections achieved within the JM17 model in several bins of $W < 1.6$ GeV for $Q^2 = 3.50$–4.20 GeV^2 are shown in Figs. 3–5(a). The chosen W intervals are closest to the Breit-Wigner masses of the $N(1440)1/2^+$, $N(1520)3/2^-$, and $\Delta(1600)3/2^+$. The following discrepancies have been observed in the description of these data:

(i) The JM17 model overestimates the π^- and p polar angular distributions for forward CM angles.
(ii) These discrepancies are correlated with overestimated π^+ angular distributions at backward CM polar angles.
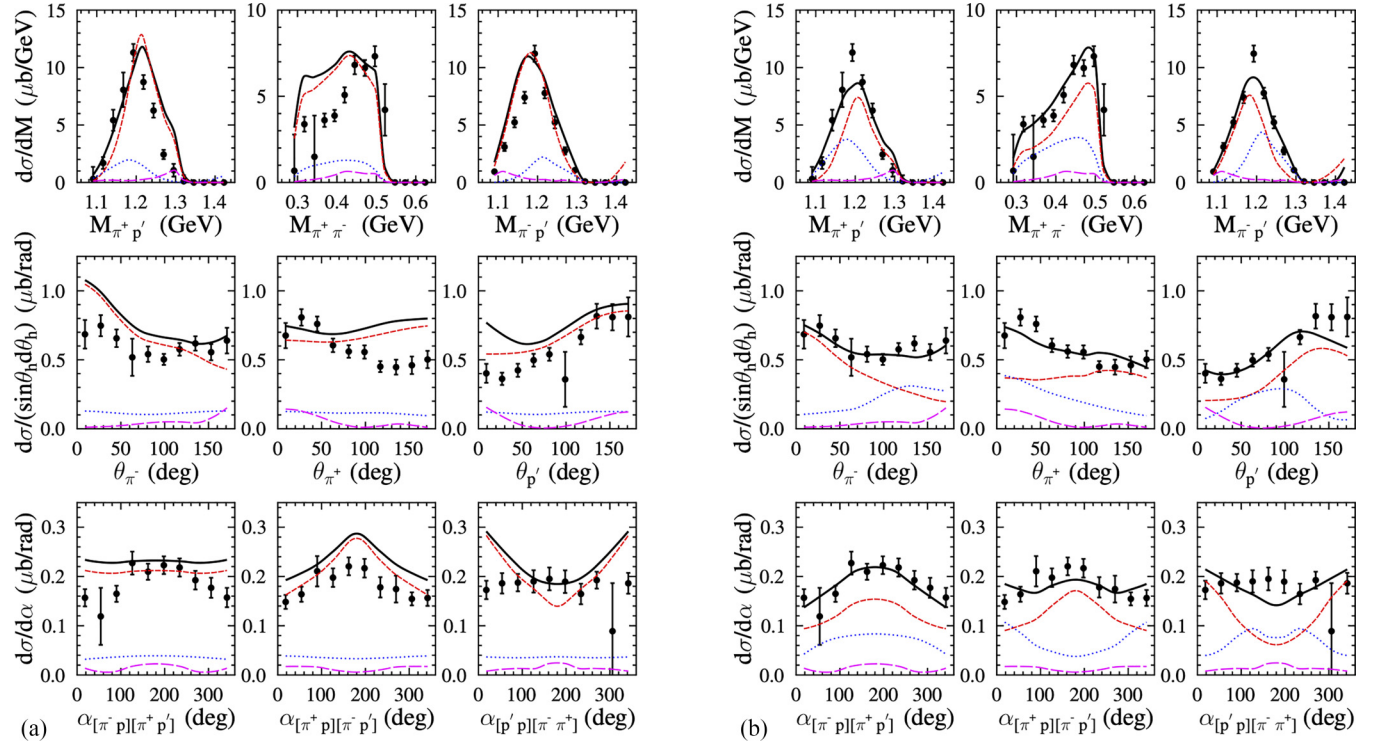
FIG. 3. Description of the nine onefold differential $\pi^+\pi^-p$ electroproduction cross sections measured with CLAS [46,47] (black points) achieved within the JM17 reaction model (a) and after improvements within the updated version JM23 (b) at $W = 1.45$–1.48 GeV and $Q^2 = 3.50$–4.20 GeV^2. θ_h represents the CM emission angles of the final state hadrons ($h = \pi^-, \pi^+, p'$). The computed differential cross sections are shown by the black solid lines, while the contributions from the $\pi^-\Delta^{++}$ and $\pi^+\Delta^0$ channels are shown by the red dashed and blue dotted lines, respectively. The contributions from direct 2π production are shown by the magenta long-dashed lines.

FIG. 4. Description of the nine onefold differential $\pi^+\pi^-p$ electroproduction cross sections measured with CLAS [46,47] (in red) achieved within the JM17 reaction model (a) and after improvements within the updated version JM23 (b) at $W = 1.50$–1.53 GeV and $Q^2 = 3.50$–4.20 GeV^2. The legend for the curves is the same as in Fig. 3.
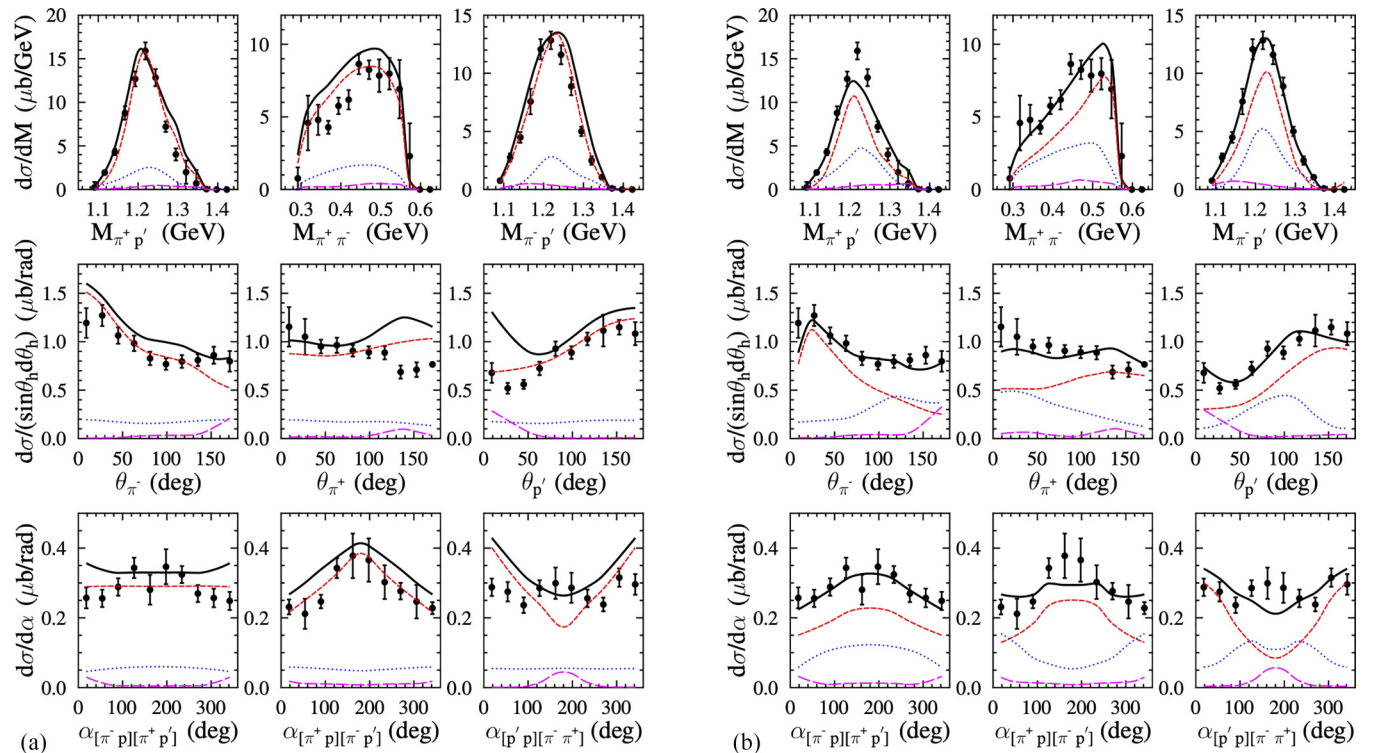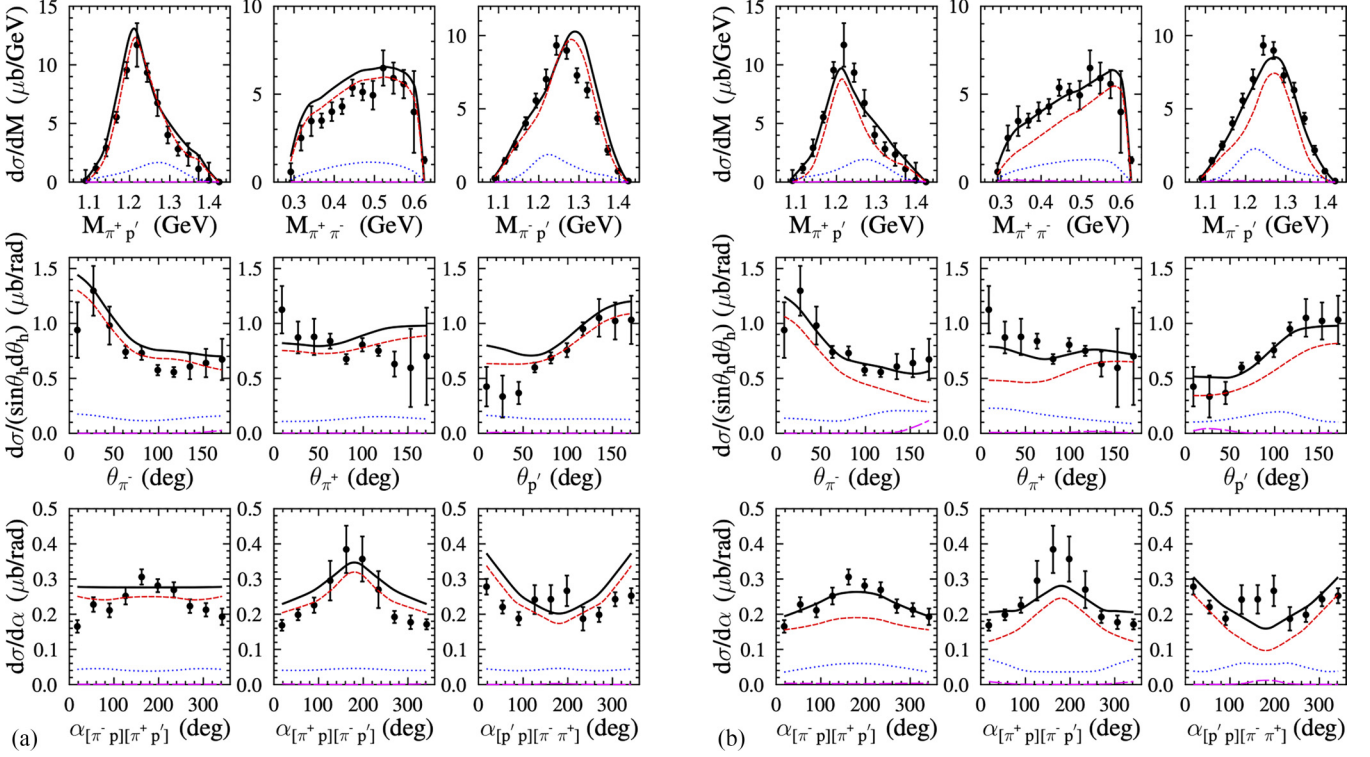
FIG. 5. Description of the nine onefold differential $\pi^+\pi^- p$ electroproduction cross sections measured with CLAS [46,47] (in red) achieved within the JM17 reaction model (a) and after improvements within the updated version JM23 (b) at $W = 1.55$–1.58 GeV and $Q^2 = 3.50$–4.20 GeV^2. The legend for the curves is the same as in Fig. 3.

(iii) Substantial deviations between the computed and measured $d\sigma/d\alpha_{[\pi^+\pi^-][pp']}$ differential cross sections become evident.

(iv) The JM17 model cannot reproduce the shape of the $\pi^+\pi^-$ invariant mass distributions for $W < 1.55$ GeV and of the $\pi^- p$ invariant mass distributions at $W < 1.50$ GeV for $Q^2 = 2.0$–5.0 GeV^2.

Comparisons of Figs. 3–5(a) demonstrate that these discrepancies are related mostly to the limitations of the JM17 model for the description of the $\pi\Delta$ channels for $Q^2 = 2.0$–5.0 GeV^2. The phenomenological extra contact terms employed for the description of the contributions into the $\pi\Delta$ amplitudes beyond the Born terms have been further modified to achieve the quality of the data description needed for the extraction of the electrocouplings.

These modifications are achieved by multiplying the extra contact term amplitudes $T^0_{\mathrm{e.c.t.}\,\pi\Delta}$ employed in the JM17 model (detailed in Ref. [18], Appendix II) with (a) the four factors $F_1(t'_{pp'})$, $F_2(t'_{\gamma\pi^-})$, $F_3(t'_{\gamma\pi^+})$, and $F_4(t'_{\gamma p'})$, which allow for a better description of the CM θ_i ($i = \pi^+, \pi^-, p'$) angular distributions of the final state hadrons, and (b) the factor $M_1(M_{\pi^+\pi^-})$ needed in order to improve the description of $\pi^+\pi^-$ invariant mass distributions. The updated extra contact term amplitudes $T_{\mathrm{e.c.t.}\,\pi\Delta}$ are parametrized as

$$
\begin{aligned}
T_{\mathrm{e.c.t.}\,\pi\Delta} = {}& T^0_{\mathrm{e.c.t.}\,\pi\Delta} F_1(t'_{pp'}) F_2(t'_{\gamma\pi^-}) \\
& \times F_3(t'_{\gamma\pi^+}) F_4(t'_{\gamma p'}) M_1(M_{\pi^+\pi^-}).
\end{aligned} \tag{1}
$$

Here $t'_{pp'}$, $t'_{\gamma\pi^-}$, $t'_{\gamma\pi^+}$, and $t'_{\gamma p'}$ are the squared four-momentum transfers defined by the difference between the initial state γ_v and p and one of the final state hadrons, and their maximum values in the respective physics regions. They are defined by

$$
t_{pp'} = (p_p - p_{p'})^2, \quad t'_{pp'} = t_{pp'} - t^{\max}_{pp'},
$$

$$
t^{\max}_{pp'} = 2m_p^2 - 2E_p E_{p'} + 2|p_p||p_{p'}|, \tag{2}
$$

$$
t_{\gamma\pi^-} = (q_\gamma - p_{\pi^-})^2, \quad t'_{\gamma\pi^-} = t_{\gamma\pi^-} - t^{\max}_{\gamma\pi^-},
$$

$$
t^{\max}_{\gamma\pi^-} = -Q^2 + m_\pi^2 - 2E_\gamma E_{\pi^-} + 2|q_\gamma||p_{\pi^-}|,
$$

$$
Q^2 = -q_\gamma^2, \tag{3}
$$

$$
t_{\gamma\pi^+} = (q_\gamma - p_{\pi^+})^2, \quad t'_{\gamma\pi^+} = t_{\gamma\pi^+} - t^{\max}_{\gamma\pi^+},
$$

$$
t^{\max}_{\gamma\pi^+} = -Q^2 + m_\pi^2 - 2E_\gamma E_{\pi^+} + 2|q_\gamma||p_{\pi^+}|, \tag{4}
$$

$$
t_{\gamma p'} = (q_\gamma - p_{p'})^2, \quad t'_{\gamma p'} = t_{\gamma p'} - t^{\max}_{\gamma p'},
$$

$$
t^{\max}_{\gamma p'} = -Q^2 + m_p^2 - 2E_\gamma E_{p'} + 2|q_\gamma||p_{p'}|. \tag{5}
$$

Here q_γ, p_{π^+}, p_{π^-}, and $p_{p'}$ are the four-momenta of the initial state photon and the final state π^+, π^-, and p, respectively, and p_p is the four-momentum of the initial state proton. q_γ^2, E_p, m_p, and m_π represent the virtual photon four-momentum squared, the initial state proton CM energy, and the masses of the proton and charged pions. E_{π^+}, E_{π^-}, $E_{p'}$, and $|p_{\pi^-}|$, $|p_{\pi^+}|$, $|p_{p'}|$ are the CM energies and absolute values of the three-momenta for the final state π^+, π^-, and p, respectively, while $|q_\gamma|$ is the absolute value of the virtual photon three-momentum in the CM frame.
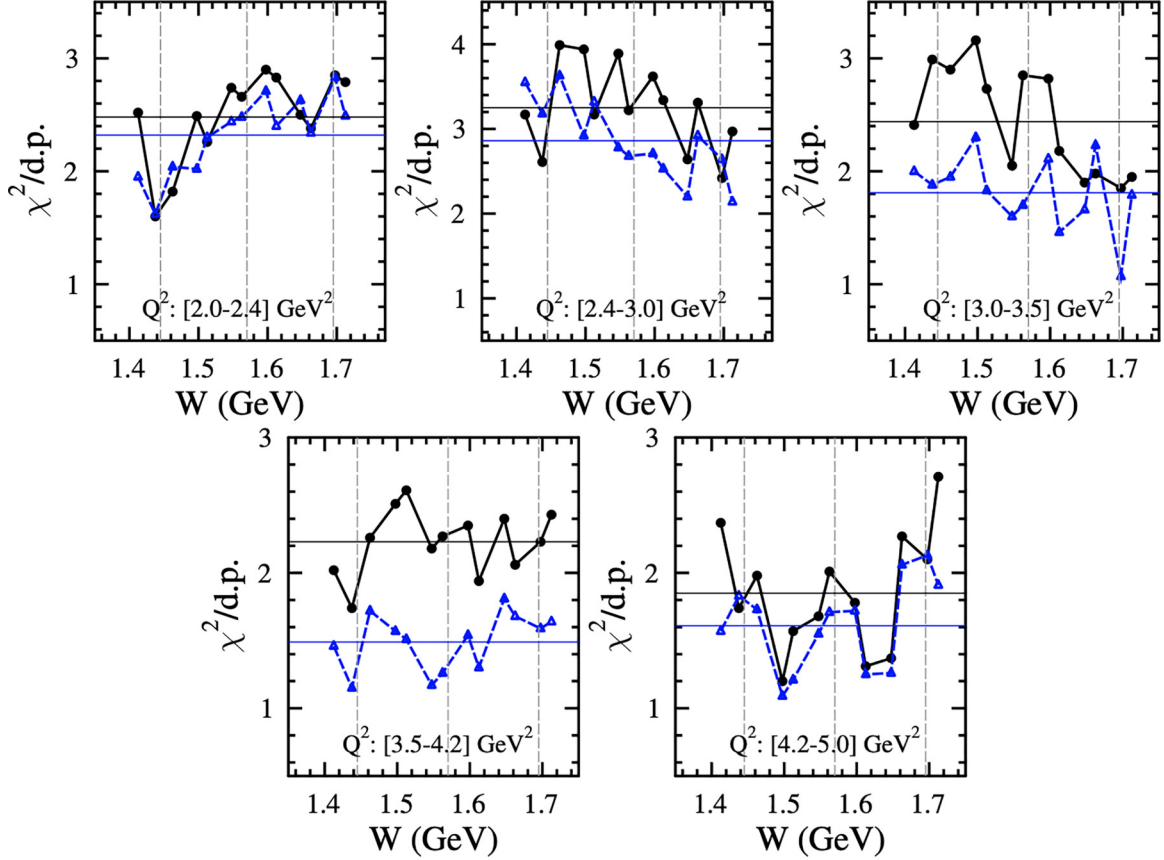
FIG. 6. Description of the nine onefold differential $\pi^+\pi^-p$ electroproduction cross sections in terms of $\chi^2/\text{d.p.}$ determined from the point-by-point comparison between the experimental data (only statistical uncertainties taken into account) and the values computed within the JM23 model as a function of W for Q^2 as indicated on the plots. $\chi^2/\text{d.p.}$ with/without implementation of the $\Delta(1600)3/2^+$ is shown by the blue/black points, respectively. The blue dashed/black solid lines connecting the points are provided only to guide the eye. The horizontal blue/black solid lines represent the average $\chi^2/\text{d.p.}$ values for each Q^2 bin with/without the $\Delta(1600)3/2^+$. The Breit-Wigner mass of the $\Delta(1600)3/2^+$ is indicated by the middle vertical line and the outer vertical lines show the total decay width.

The factors F_j in Eq. (1) are parametrized as

$$F_j = \begin{cases} -t'_j & \text{if } t_j > \Lambda_j(W, Q^2), \\ \Lambda_j(W) - t_j^{\max} & \text{if } t_j < \Lambda_j(W, Q^2), \end{cases} \quad (6)$$

where $j = pp', \gamma\pi^-, \gamma\pi^+, \gamma p'$ and the parameters $\Lambda_j(W, Q^2)$ are adjusted to reproduce the data on the CM π^+, π^-, and p angular distributions in each bin of W and Q^2 independently.

The F_i factors make the extra contact term contributions equal to zero at the maximum accessible values of the respective squared four-momentum transfers. They cause the amplitudes to increase with $-t'_j$ (or with absolute t'_j values) in the range of $t'_j > \Lambda_j$, making the final state hadron CM angular distributions closer to those measured with CLAS.

The factor $M_1(M_{\pi^+\pi^-})$ in Eq. (1) is essential to improve the description of the $\pi^+\pi^-$ invariant mass distributions. It is given by

$$M_1(M_{\pi^+\pi^-}) = \begin{cases} \dfrac{M_{\pi^+\pi^-}^2 - a_{\pi^+\pi^-}(W, Q^2)m_\pi^2}{[W - b_{\pi^+\pi^-}(W, Q^2)M_p]^2 - M_{\pi^+\pi^-}^2} & \text{if } W < 1.6 \text{ GeV}, \\ 1 & \text{if } W > 1.6 \text{ GeV}, \end{cases}$$

$$\quad (7)$$

where the parameters $a_{\pi^+\pi^-}(W, Q^2)$ $(a_{\pi^+\pi^-} > 4.0)$ and $b_{\pi^+\pi^-}(W, Q^2)$ $(0.0 < b_{\pi^+\pi^-} < 1.0)$ are adjusted to the data in each bin of W and Q^2 independently. At values of $b_{\pi^+\pi^-}(W, Q^2)$ equal to unity, the factor $M_1(M_{\pi^+\pi^-})$ develops a pole at the maximum kinematically allowed invariant masses $M_{\pi^+\pi^-}$. Hence, the denominator in Eq. (7) defines the shape of the $M_{\pi^+\pi^-}$ invariant mass distributions at their largest kinematically allowed values, while the numerator in Eq. (7) regulates the slope of the $M_{\pi^+\pi^-}$ mass distributions.

The modifications of the JM17 model extra contact term described above and the implementation of the $\Delta(1600)3/2^+$ led to the updated model version referred to as JM23. With the JM23 model, a reasonable description of the experimental data on the nine independent onefold differential $\pi^+\pi^-p$ electroproduction cross sections has been achieved in the extended Q^2 range as exemplified in Figs. 3–5(b). The $\chi^2/\text{d.p.}$ (d.p. = data point) values computed within the range of $W < 1.7$ GeV for $Q^2 = 2.0$–5.0 GeV^2 from the point-by-point comparison between the measured $\pi^+\pi^-p$ differential cross sections and those evaluated within JM23 are shown in Fig. 6 as a function of W in each Q^2 interval covered by the analyzed CLAS data. Only the statistical data uncertainties were included in the evaluation of $\chi^2/\text{d.p.}$ to enhance the sensitivity of these

quantities to the parametrization of nonresonant contributions. In each bin the χ^2/d.p. values are comparable with those achieved in previous analyses of $\pi^+\pi^- p$ electroproduction data [11,12] where the electrocouplings were deduced from the data fits within the previous versions of the JM model. From six to eight parameters of the nonresonant amplitudes were varied in the extraction of the $\gamma_v p N^*$ electrocouplings, which were fit to 102 data points in each bin of (W, Q^2). The resonance electrocouplings presented in this paper have been determined from the $\pi^+\pi^- p$ electroproduction data fit within the JM23 model.

We also explored the impact of the $\Delta(1600)3/2^+$ on the description of the $\pi^+\pi^- p$ differential cross sections. The four-star status for this state was assigned after 2017, hence it was not included in the JM17 model. The $\Delta(1600)3/2^+$ was incorporated into the JM23 version with starting hadronic decay parameters taken from the PDG [14] and with the initial $\gamma_v p N^*$ electrocouplings from the CSM predictions [51]. The results in Fig. 6 demonstrate improvements in the description of the $\pi^+\pi^- p$ differential cross sections after implementation of this state. The improvements become more pronounced with increasing Q^2, suggesting a relative increase of the signal from the $\Delta(1600)3/2^+$ with Q^2. For the highest Q^2 bin, because of the increase of the data uncertainties, the improvement of the data description is less pronounced. It is also worth noting that the implementation of the $\Delta(1600)3/2^+$ into JM23 has allowed for the reduction of the magnitudes of the direct 2π production amplitudes by 20–50% and for the extra contact term amplitudes in the $\pi\Delta$ subchannels by 10–30%, which represent the contributions described within the entirely phenomenological parametrization. These observations have confirmed the impact of the $\Delta(1600)3/2^+$ contribution in $\pi^+\pi^- p$ electroproduction.

III. RESONANCE PARAMETER EXTRACTION FROM CROSS SECTION FITS

The electrocouplings of the $N(1440)1/2^+$, $N(1520)3/2^-$, and $\Delta(1600)3/2^+$, as well as their branching fractions for decays into $\pi\Delta$ and ρp, were extracted from fits of the nine independent onefold differential $\pi^+\pi^- p$ cross sections as described in Sec. II A. A good description of the $\pi^+\pi^- p$ electroproduction data achieved with the JM23 model at $W < 1.7$ GeV for $Q^2 = 2.0$–5.0 GeV^2 allows for the determination of the resonance parameters from the data fit for $W = 1.40$–1.66 GeV and $Q^2 = 2.0$–5.0 GeV^2. The electrocouplings and hadronic decay parameters were obtained from independent fits within the three overlapping W intervals given in Table IV. The nonresonant contributions in these W intervals are different, while the electrocouplings determined from the data fits should be the same within their uncertainties, validating extraction of these quantities.

In the data fit we simultaneously varied the electrocouplings, the resonance partial decay widths into $\pi\Delta$ and ρp, and the Breit-Wigner masses for all N^* states listed in Table III. The starting values for the resonance decay amplitudes into $\pi\Delta$ and ρp of orbital angular momentum L and total spin

TABLE IV. W intervals where the nine independent onefold differential $\pi^+\pi^- p$ electroproduction cross sections were fit independently for $Q^2 = 2.0$–5.0 GeV^2 to extract the $N(1440)1/2^+$, $N(1520)3/2^-$, and $\Delta(1600)3/2^+$ electrocouplings and their BF for decays into the $\pi\Delta$ and ρp intermediate states with JM23.

Resonance	W interval (GeV)
$N(1440)1/2^+$	1.41–1.51
	1.46–1.56
	1.51–1.61
$N(1520)3/2^-$	1.41–1.51
	1.46–1.56
	1.51–1.61
$\Delta(1600)3/2^+$	1.46–1.56
	1.51–1.61
	1.56–1.66

S, are defined by

$$\sqrt{\Gamma_{LS}^i} = \sqrt{\Gamma_{tot} BF_{LS}^i},\qquad(8)$$

where the resonance total decay widths Γ_{tot} were taken from Ref. [14], and the branching fractions BF_{LS}^i ($i = \pi\Delta, \rho p$) for the $N(1440)1/2^+$ and $N(1520)3/2^-$ were taken from the previous studies of CLAS πN and $\pi^+\pi^- p$ electroproduction data [10–12]. For other excited states, the outcome of the analyses of Refs. [56,57] were used for the BF_{LS}^i starting values. For each resonance, the total decay width was computed as the sum of all partial decay widths. The floating of the resonance masses and total decay widths Γ_{tot} caused by variation of the partial hadronic decay widths into $\pi\Delta$ and ρp were limited by the intervals given in Ref. [14]. In this way, we imposed restrictions for the variation of the N^* partial hadronic decay widths Γ_{LS}^i ($i = \pi\Delta, \rho p$) into $\pi\Delta$ and ρp decomposed over the LS partial waves.

The starting values for the $N(1440)1/2^+$ and $N(1520)3/2^-$ electrocouplings used in the fit of the $\pi^+\pi^- p$ electroproduction cross sections were taken from the analysis of πN electroproduction [10]. The transverse electrocouplings $A_{1/2}$ and $A_{3/2}$ of these states were varied by employing normal distributions with the σ parameters equal to 30% of their starting values. There were no restrictions on the minimum or maximum trial electrocoupling values, allowing us to explore the area of $\approx \pm 3\sigma$ around the starting values. The longitudinal $S_{1/2}$ electrocouplings of smaller absolute values were varied within a broader range so that their absolute values overlapped with the absolute values of the transverse electrocouplings.

The starting values for the electrocouplings of the $\Delta(1600)3/2^+$ were based on the CSM predictions [51]. Currently, CSM takes into account only the contributions from the quark core that gradually dominate as Q^2 increases, typically for $Q^2 \gtrsim 2$ GeV^2, which is the range covered in this analysis. Therefore, the actual starting values of the $\Delta(1600)3/2^+$ electrocouplings were taken from the values of Ref. [51] multiplied by a common factor of 0.6 applied over the entire range of Q^2 for all three electrocouplings $A_{1/2}$, $A_{3/2}$, and $S_{1/2}$. This factor accounts for the fact that the wave function of the $\Delta(1600)3/2^+$ represents a superposition of the contributions

from the quark core and meson-baryon cloud. In the data fit, implementation of this factor was needed to reproduce the results on the final state proton CM angular distributions in the forward hemisphere. The $\Delta(1600)3/2^+$ electrocouplings were varied employing normal distributions with the σ parameters equal to 50% of their starting values.

In the fits we simultaneously varied the electrocouplings of all N^*'s of four-star status [other than the $N(1440)1/2^+$, $N(1520)3/2^-$, and $\Delta(1600)3/2^+$] as described above within the mass range below 1.7 GeV. This variation employed a normal distribution with the σ parameters equal to 20% of their starting values, which were taken from the analyses of the CLAS exclusive meson electroproduction data [1] with the numerical results available in Ref. [30].

In the data fit we also varied the following parameters of the nonresonant mechanisms employed in the JM23 model:

(i) the magnitudes of the additional contact-term amplitudes in the $\pi^-\Delta^{++}$ and $\pi^+\Delta^0$ channels (1 parameter per Q^2 bin);

(ii) the magnitudes of the $\pi^+N^0(1520)3/2^-$ channel (1 parameter per Q^2 bin);

(iii) the magnitudes of all direct 2π production amplitudes (up to six parameters per Q^2 bin).

The starting values for these parameters were determined in their initial adjustment to the nine independent onefold $\pi^+\pi^-p$ differential cross sections. We applied W-independent multiplicative factors to the magnitudes of the nonresonant amplitudes listed above. They remained the same in the entire W interval covered by the fit within any Q^2 bin, but they depended on Q^2 and were fit to the data in each Q^2 bin independently. The multiplicative factors were varied around unity, employing normal distributions with σ values in the range of 20%. In this way, we retained a smooth W dependence of the nonresonant contributions established in the adjustment to the data and explored the possibility of improving the data description in the simultaneous variation of the resonant and nonresonant parameters.

The special data fit procedure described in Ref. [11] was employed for the extraction of the resonance parameters. It allowed us to obtain not only the best fit but also to establish bands of the computed cross sections that were compatible with the data within their uncertainties. For each trial set of JM23 resonant and nonresonant parameters, we computed the nine onefold differential $\pi^+\pi^-p$ cross sections and $\chi^2/$d.p. values. The latter were estimated in point-by-point comparisons between the measured and computed cross sections in all bins of $W = 1.41$–1.66 GeV for $Q^2 = 2.0$–5.0 GeV^2 covered by the CLAS data. The data uncertainties account for both the statistical and that part of the systematic uncertainty dependent on the final state hadron kinematics, which were added in quadrature. In the fit, we selected the computed onefold differential cross sections closest to the data with $\chi^2/$d.p. less than a predetermined maximum value. These values of $\chi^2_{max}/$d.p. were obtained by requiring that the computed cross sections with smaller $\chi^2/$d.p. be within the data uncertainties for the majority of the data points. In this fit procedure, we obtained the $\chi^2/$d.p. intervals within which the computed

TABLE V. The ranges of $\chi^2/$d.p. for the nine onefold differential $\pi^+\pi^-p$ electroproduction cross sections selected in the data fit computed within JM23 in overlapping W intervals for $Q^2 = 2.0$–5.0 GeV^2. The uncertainties for the measured data are given by the quadratic sum of the statistical and that part of the systematic uncertainty dependent on the final state hadron kinematics.

W interval (GeV)	1.41–1.51	1.46–1.56	1.51–1.61	1.56–1.66
$\chi^2/$d.p. range	0.51–0.57	0.52–0.67	0.52–0.69	0.69–0.76

cross sections described the data equally well within the data uncertainties. The ranges of $\chi^2/$d.p. listed in Table V demonstrate that the cross sections selected in the data fit are indeed distributed within the data uncertainties over the entire area of (W, Q^2) covered in the data analysis.

Representative examples for the fit quality of the cross sections within the W intervals closest to the Breit-Wigner masses of the $N(1440)1/2^+$, $N(1520)3/2^-$, and $\Delta(1600)3/2^+$ for $Q^2 = 3.0$–3.5 GeV^2 are shown in Fig. 7. The computed cross sections selected in the data fit are shown by the red curves. The resonant contributions were obtained from the differential cross sections computed from only the resonance amplitudes and are shown by the blue bars. The deduced uncertainties for the resonance contributions are comparable both with the uncertainties of the measured differential cross sections and with the spread of the fits computed within the JM23 model. Pronounced differences are evident in the shapes of the computed differential cross sections selected in the data fit and the respective resonant contributions, in particular for all angular distributions. The shapes of the resonant contributions are different in each of the nine onefold differential cross sections but they are highly correlated by the reaction dynamics that underlie the resonance excitations in the s channel and their subsequent decays into either the $\pi\Delta$ or ρp intermediate states. The resonant/nonresonant contribution differences allow for isolation of the resonant contributions. The electrocouplings and decay widths into $\pi\Delta$ and ρp have been determined from the resonant contributions by fitting them within the unitarized Breit-Wigner ansatz [11,52], taking into account the constraints imposed on the resonant amplitudes by a general unitarity condition.

IV. $N(1440)1/2^+$, $N(1520)3/2^-$, AND $\Delta(1600)3/2^+$ ELECTROCOUPLINGS AND HADRONIC DECAY WIDTHS TO $\pi\Delta$ AND ρp

The resonance parameters determined from the data fit include the electrocouplings, the partial decay widths into $\pi\Delta$ and ρp, and the total resonance decay widths. They are averaged from the group of fits selected by the $\chi^2/$d.p. limits and their mean values are taken as the resonance parameters extracted from the data. The root-mean-square dispersions in these parameters are taken as the uncertainties. The electrocoupling uncertainties obtained in this manner take into account both the statistical and systematic uncertainties in the data, as well as the systematic uncertainties associated with the JM23 model. Furthermore, we consistently account for the correlations between the variations of the resonant
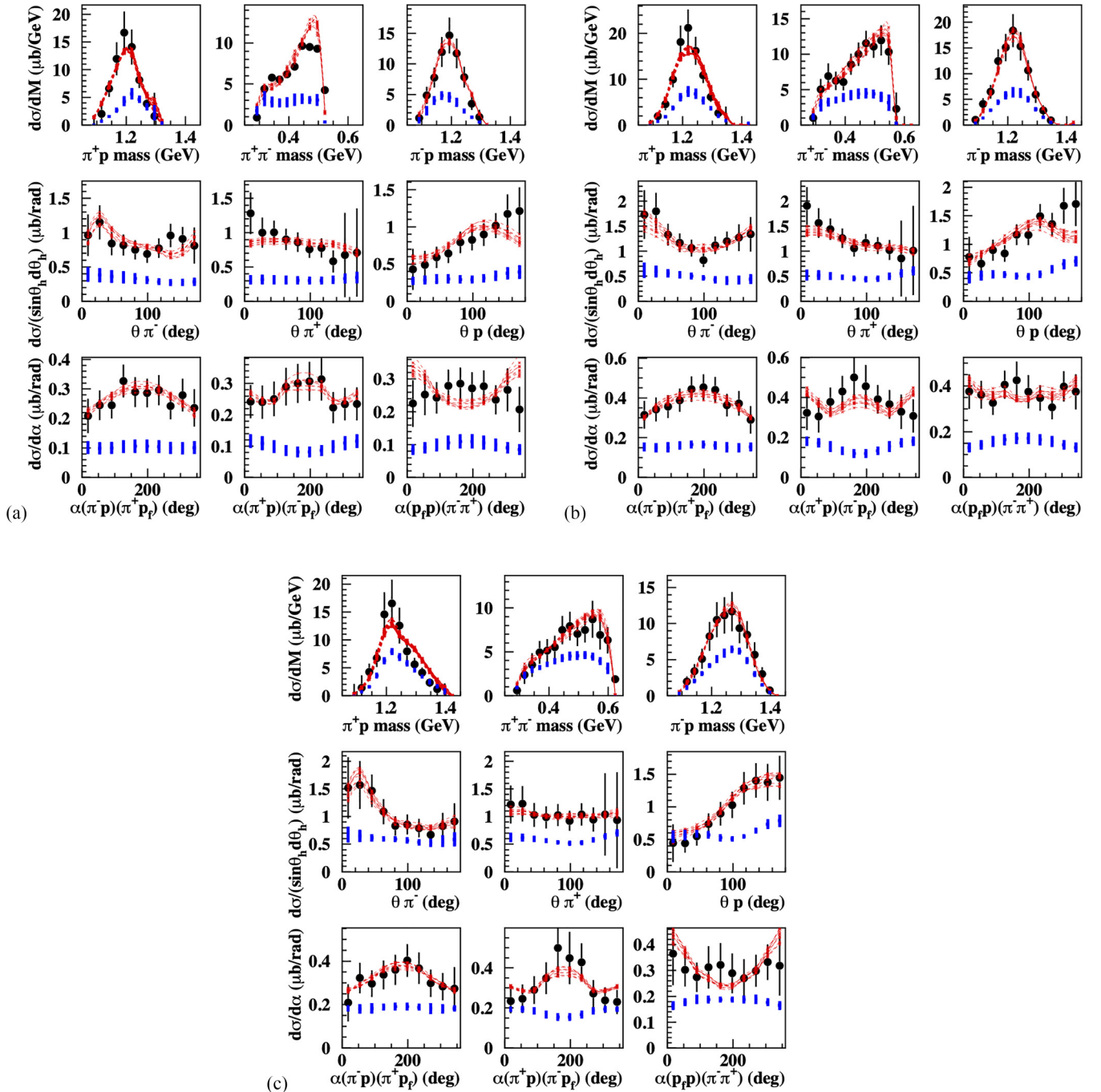
FIG. 7. Fit of the nine onefold differential $\pi^+\pi^- p$ electroproduction cross sections measured with CLAS [47] (in black) achieved within the JM23 model for $W = 1.450$–1.475 GeV (a), 1.500–1.525 GeV, (b) and 1.550–1.575 GeV (c) for $Q^2 = 3.0$–3.5 GeV^2. The data point uncertainties are evaluated as a quadratic sum of statistical and relevant systematic uncertainties. The groups of red curves represent the JM23 fits closest to the data. The resonant contributions are shown in blue.

and nonresonant contributions when extracting the resonance parameters. In the cases where the ranges of the extracted electrocouplings covered more than 90% of the intervals for the electrocoupling variation (starting values $\pm\sigma$) employed in the data fit, we further increased the ranges of the variation and repeated the data fit, so that eventually the electrocouplings extracted from the data were inside the intervals of the variations employed in the data fit. In this way, we made sure that the employed ranges were sufficient to determine both the mean values of the resonance parameters and their uncertainties.

A. Parameters for the $N(1440)1/2^+$ and $N(1520)3/2^-$

The hadronic decay widths of the $N(1440)1/2^+$ and $N(1520)3/2^-$ were deduced from the fits of the $\pi^+\pi^- p$

TABLE VI. Masses and total/partial hadronic decay widths of the $N(1440)1/2^+$ into $\pi\Delta$ and ρp determined from fits of the $\pi^+\pi^- p$ electroproduction cross sections carried out independently within different Q^2 intervals. The new results from this work are given in the last two rows. The results in the upper rows are available from previous studies [11,12] of the $\pi^+\pi^- p$ electroproduction cross sections.

Q^2 interval (GeV^2)	Mass (GeV)	Γ_{tot} (MeV)	$\Gamma_{\pi\Delta}$ (MeV)	BF$_{\pi\Delta}$ (%)	$\Gamma_{\rho p}$ (MeV)	BF$_{\rho p}$ (%)
0.25–0.60	1.458 ± 0.012	363 ± 39	142 ± 48	23–58	6 ± 4	<2
0.5–1.5	1.450 ± 0.011	352 ± 37	120 ± 41	20–52	5 ± 2	<2
2.0–3.5	1.457 ± 0.008	331 ± 54	129 ± 52	20–65	6 ± 2	1.1–2.6
3.0–5.0	1.446 ± 0.013	352 ± 33	151 ± 32	31–57	5 ± 1	1.2–2.0

differential cross sections using the procedures described in Sec. III. The results are presented in Table VI for the $N(1440)1/2^+$ and in Table VII for the $N(1520)3/2^-$. For both resonances, their masses and total/partial hadronic decay widths into $\pi\Delta$ and ρp are self-consistent in the four Q^2 intervals covered by the CLAS $\pi^+\pi^- p$ electroproduction cross sections from the previous studies [11,12] and those reported in this work. The successful fit of the data achieved within a broad range of $Q^2 = 0.25$–5.0 GeV^2 with Q^2-independent resonance masses and total/partial hadronic decay widths given the pronounced evolution of the nonresonant mechanisms with Q^2, demonstrates that both the $N(1440)1/2^+$ and $N(1520)3/2^-$ are excited states of the proton produced in the s channel for the $\gamma_v p$ interaction.

The electrocouplings for the $N(1440)1/2^+$ and $N(1520)3/2^-$ determined from the fits of the $\pi^+\pi^- p$ cross sections carried out independently in three overlapping W intervals for $Q^2 = 2.0$–5.0 GeV^2 are shown in Figs. 8 and 9, respectively. The nonresonant contributions in these three W intervals are different, however the extracted electrocouplings are consistent within the uncertainties, suggesting credible extraction of these quantities.

In order to compare results for the $N(1440)1/2^+$ and $N(1520)3/2^-$ electrocouplings in the $\pi^+\pi^- p$ electroproduction channel with the values from the analysis of πN electroproduction, we must use common decay branching fractions to these final states for each resonance. Within the JM23 model, the sum of the branching fractions into πN and $\pi\pi N$ accounts for almost 100% of the total decay widths of the $N(1440)1/2^+$ and $N(1520)3/2^-$. Since the πN exclusive electroproduction channels are the most sensitive to contributions from the $N(1440)1/2^+$ and $N(1520)3/2^-$, we reevaluated the branching fraction for the decay to the $\pi\pi N$

final states BF$(\pi\pi N)_{\text{corr}}$ as

$$\text{BF}(\pi\pi N)_{\text{corr}} = 1 - \text{BF}(\pi N). \quad (9)$$

For these resonance decays to $\pi\pi N$, it turns out that the estimated branching fractions BF$(\pi\pi N)_{\text{corr}}$ are slightly (<10%) different with respect to those obtained from the $\pi^+\pi^- p$ fit [BF$(\pi\pi N)_0$]. Therefore, we multiplied the $\pi\Delta$ and ρp hadronic decay widths of the $N(1440)1/2^+$ and $N(1520)3/2^-$ from the $\pi^+\pi^- p$ fit by the ratio $\frac{\text{BF}(\pi\pi N)_{\text{corr}}}{\text{BF}(\pi\pi N)_0}$. The electrocouplings obtained were then multiplied by the correction factors

$$C_{hd} = \sqrt{\frac{\text{BF}(\pi\pi N)_{\text{corr}}}{\text{BF}(\pi\pi N)_0}} \quad (10)$$

in order to keep the resonant parts and the computed $\pi^+\pi^- p$ differential cross sections unchanged under the re-scaling of the resonance hadronic decay parameters described above.

A special procedure was developed for the evaluation of the transverse A_i ($i = 1/2, 3/2$) and longitudinal S_i ($i = 1/2$) electrocouplings analyzing the results from independent fits of the electroproduction cross sections in the three W intervals with electrocouplings and uncertainties $A_{i,j} \pm \delta A_{i,j}$ and $S_{i,j} \pm \delta S_{i,j}$, where the index $j = 1 \to 3$ is the W interval. First, we found the overlap range for the electrocouplings $[A_i^{\min} - A_i^{\max}]$ ($i = 1/2, 3/2$) and $[S_i^{\min} - S_i^{\max}]$ ($i = 1/2$) from the data fit in the three W intervals:

$$A_i^{\min} = \min[A_{i,j} + \delta A_{i,j}], \quad S_i^{\min} = \min[S_{i,j} + \delta S_{i,j}],$$
$$A_i^{\max} = \max[A_{i,j} - \delta A_{i,j}], \quad S_i^{\max} = \max[S_{i,j} - \delta S_{i,j}]. \quad (11)$$

Within these ranges the best data description was achieved in all W intervals. Consequently, the mean values for A_i and S_i

TABLE VII. Masses and total/partial hadronic decay widths of the $N(1520)3/2^-$ into $\pi\Delta$ and ρp determined from fits of the $\pi^+\pi^- p$ electroproduction cross sections carried out independently within different Q^2 intervals. The new results from this work are given in the last two rows. The results in the upper rows are available from previous studies [11,12] of the $\pi^+\pi^- p$ electroproduction cross sections.

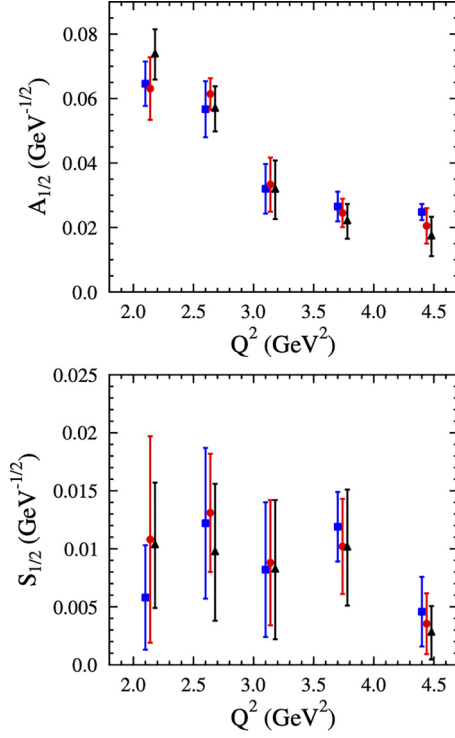| Q^2 interval (GeV^2)	Mass (GeV)	Γ_{tot} (MeV)	$\Gamma_{\pi\Delta}$ (MeV)	BF$_{\pi\Delta}$ (%)	$\Gamma_{\rho p}$ (MeV)	BF$_{\rho p}$ (%)
0.25–0.60	1.521 ± 0.004	127 ± 4	35 ± 4	24–32	16 ± 5	8–17
0.5–1.5	1.520 ± 0.001	125 ± 4	36 ± 5	25–34	13 ± 6	5–16
2.0–3.5	1.518 ± 0.003	122 ± 7	29 ± 5	19–30	15 ± 6	7–18
3.0–5.0	1.522 ± 0.003	121 ± 7	30 ± 5	20–30	13 ± 5	6–16

FIG. 8. Electrocouplings of the $N(1440)1/2^+$ determined from independent fits of the $\pi^+\pi^- p$ electroproduction cross sections in three W intervals, 1.41–1.51 GeV (blue squares), 1.46–1.56 GeV (red circles), and 1.51–1.61 GeV (black triangles), for $Q^2 = 2.0$–5.0 GeV^2 within the JM23 model.

were redefined as

$$A_i = \frac{A_i^{\min} + A_i^{\max}}{2} \quad (i = 1/2, 3/2),$$

$$S_i = \frac{S_i^{\min} + S_i^{\max}}{2} \quad (i = 1/2). \tag{12}$$

There are three sources of uncertainties in the evaluation of A_i and S_i in each of the three W intervals: (a) the range of overlap between the electrocouplings determined from the data fit defined in Eq. (11), (b) the root mean square (RMS) for the mean values of the determined electrocouplings, i.e., RMS$[A_{i,j}]$ and RMS$[S_{i,j}]$, and (c) the differences between the redefined electrocouplings according to Eq. (12) and their average values obtained from the data fit. The total uncertainties were obtained as the quadrature sum of the contributions (a) to (c),

$$\delta A_i = \sqrt{\frac{\left(A_i^{\max} - A_i^{\min}\right)^2}{4} + (\text{RMS}[A_{i,j}])^2 + \Delta A_i^2},$$

$$\Delta A_i = \frac{A_i^{\min} + A_i^{\max}}{2} - \frac{\sum_{j=1,2,3} A_{i,j}}{3},$$

$$\delta S_i = \sqrt{\frac{\left(S_i^{\max} - S_i^{\min}\right)^2}{4} + (\text{RMS}[S_{i,j}])^2 + \Delta S_i^2},$$

$$\Delta S_i = \frac{S_i^{\min} + S_i^{\max}}{2} - \frac{\sum_{j=1,2,3} S_{i,j}}{3}. \tag{13}$$
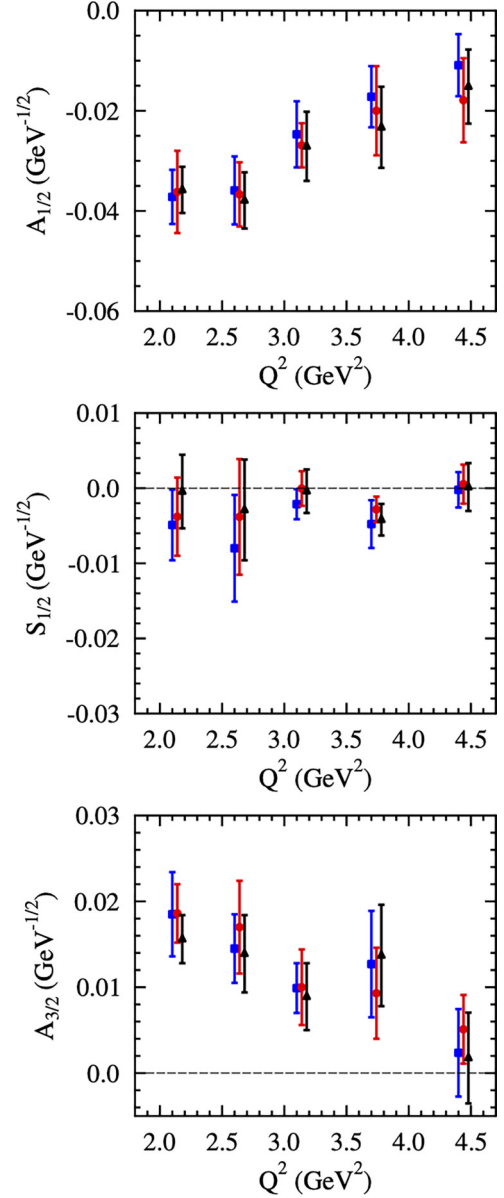

FIG. 9. Electrocouplings of the $N(1520)3/2^-$ determined from independent fits of the $\pi^+\pi^- p$ electroproduction cross sections in three W intervals, 1.41–1.51 GeV (blue squares), 1.46–1.56 GeV (red circles), and 1.51–1.61 GeV (black triangles), for $Q^2 = 2.0$–5.0 GeV^2 within the JM23 model.

The electrocouplings determined for the $N(1440)1/2^+$ and $N(1520)3/2^-$ are listed in Tables VIII and IX, respectively. We consider these results as the final electrocouplings from the analysis of the $\pi^+\pi^- p$ electroproduction cross sections within the JM23 model.

In Figs. 10 (left) and 11 (left) we compare the electrocouplings of the $N(1440)1/2^+$ and $N(1520)3/2^-$ obtained from analyses of πN electroproduction cross sections, beam, target, and beam-target asymmetries within the unitary isobar model and dispersion relation approach [10,59] with the results available from analysis of the nine independent onefold differential $\pi^+\pi^- p$ electroproduction cross sections within JM23. The

TABLE VIII. $N(1440)1/2^+$ electrocouplings determined from the $\pi^+\pi^-p$ differential cross sections measured with the CLAS detector [46,47] in three W intervals, 1.41–1.51 GeV, 1.46–1.56 GeV, and 1.51–1.61 GeV, for $Q^2 = 2.0$–5.0 GeV^2 evaluated according to Eqs. (12) and (13).

Q^2 interval (GeV^2)	$A_{1/2} \times 1000$ (GeV$^{-1/2}$)	$S_{1/2} \times 1000$ (GeV$^{-1/2}$)
2.0–2.4	68.7 ± 6.6	7.6 ± 4.1
2.4–3.0	60.2 ± 4.9	11.8 ± 4.2
3.0–3.5	32.3 ± 7.5	8.7 ± 5.3
3.5–4.2	24.6 ± 3.6	11.6 ± 3.0
4.2–5.0	22.8 ± 4.3	3.3 ± 2.0

TABLE IX. $N(1520)3/2^-$ electrocouplings determined from the $\pi^+\pi^-p$ differential cross sections measured with the CLAS detector [46,47] in three W intervals, 1.41–1.51, 1.46–1.56, and 1.51–1.61 GeV, for $Q^2 = 2.0$–5.0 GeV^2 evaluated according to Eqs. (12) and (13).

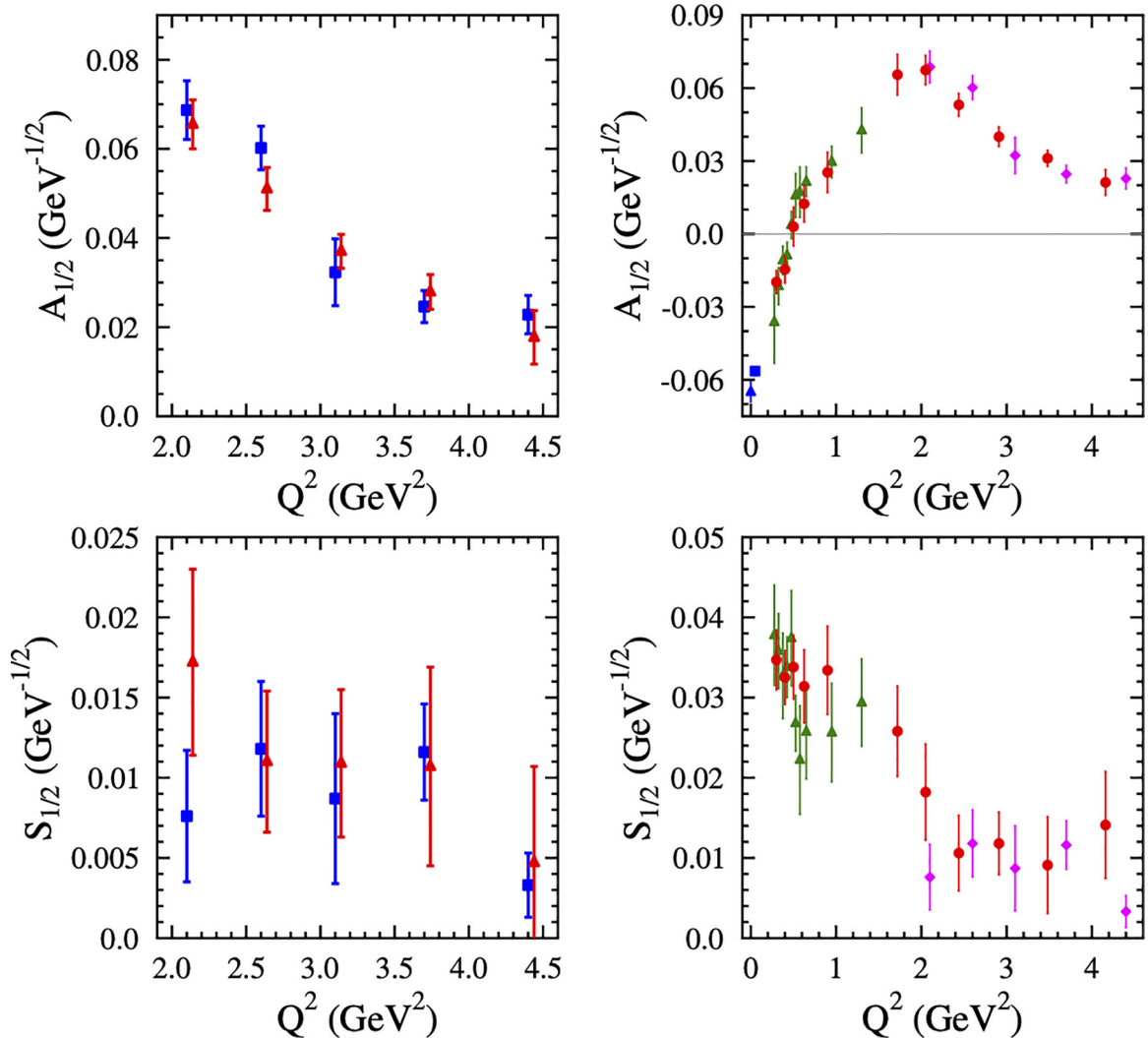| Q^2 interval (GeV^2)	$A_{1/2} \times 1000$ (GeV$^{-1/2}$)	$S_{1/2} \times 1000$ (GeV$^{-1/2}$)	$A_{3/2} \times 1000$ (GeV$^{-1/2}$)
2.0–2.4	-35.8 ± 4.8	-3.8 ± 5.4	16.8 ± 2.2
2.4–3.0	-37.5 ± 5.2	-4.1 ± 5.6	15.8 ± 3.2
3.0–3.5	-25.7 ± 3.5	-0.1 ± 2.4	9.0 ± 3.5
3.5–4.2	-16.8 ± 5.2	-3.3 ± 1.4	11.2 ± 4.3
4.2–5.0	-15.6 ± 6.7	-0.5 ± 3.0	7.0 ± 4.1

FIG. 10. Left: $N(1440)1/2^+$ electrocouplings determined from the πN differential cross sections, beam, target, and beam-target asymmetries [10] (red triangles) and from the $\pi^+\pi^-p$ differential cross sections (blue squares) for $Q^2 = 2.0$–5.0 GeV^2 presented in this work. The electrocouplings from the πN data after interpolation over Q^2 are compared with the results from the $\pi^+\pi^-p$ data. Right: $N(1440)1/2^+$ electrocouplings from the πN and $\pi^+\pi^-p$ data for $Q^2 = 0.25$–5.0 GeV^2. The results from πN electroproduction [10] are shown by the red circles. The electrocouplings from the $\pi^+\pi^-p$ differential cross sections measured with CLAS for $Q^2 = 0.25$–1.5 GeV^2 [11,12] are shown by the green triangles. The electrocouplings determined within the JM23 model are shown by the magenta diamonds. The photocouplings from the PDG [14] and from the CLAS πN photoproduction data [58] are shown by the blue triangle and square, respectively.
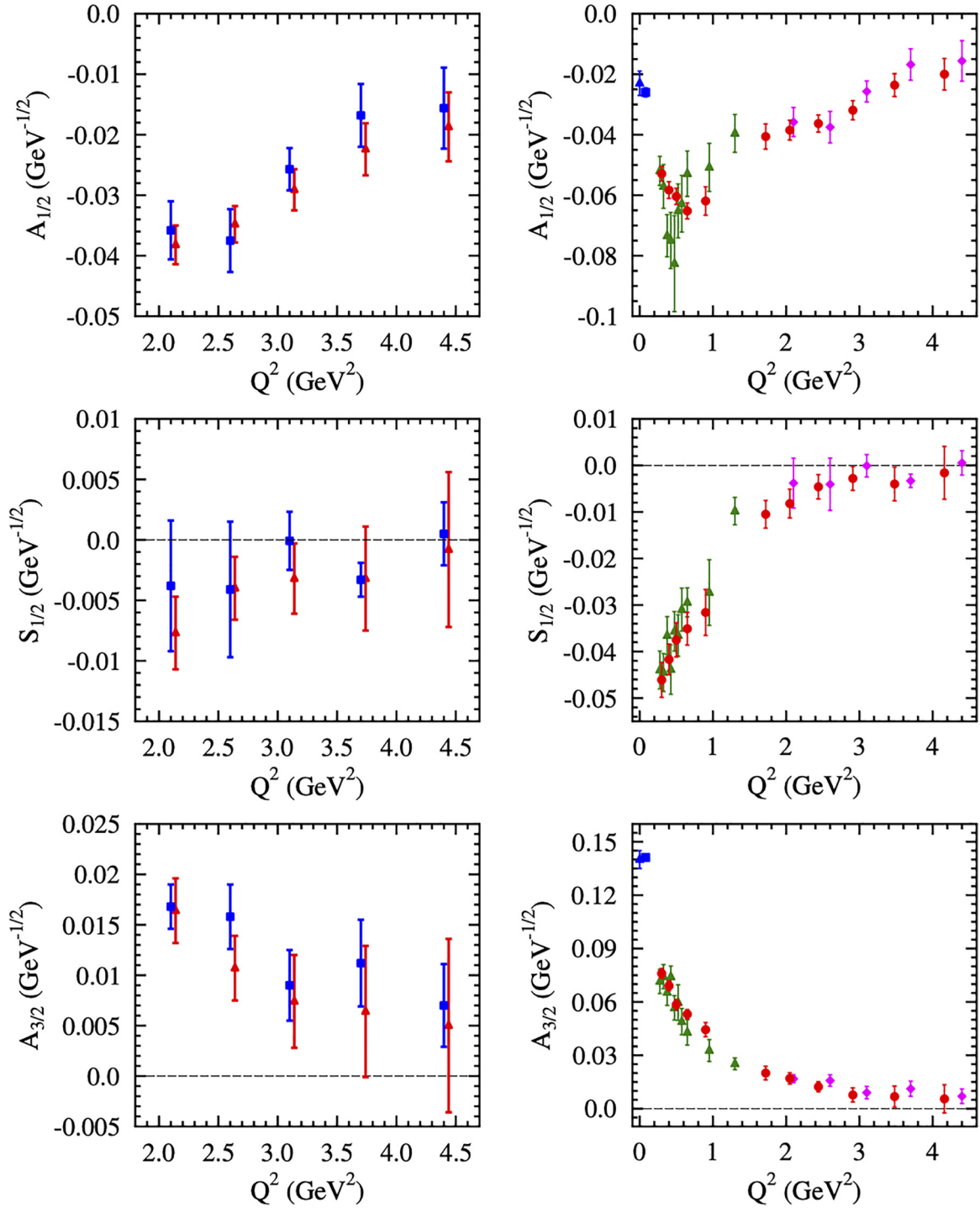
FIG. 11. Left: $N(1520)3/2^-$ electrocouplings determined from the πN differential cross sections, beam, target, and beam-target asymmetries [10] (red triangles) and from the $\pi^+\pi^- p$ differential cross sections (blue squares) for $Q^2 = 2.0$–5.0 GeV^2 presented in this work. The electrocouplings from the πN data after interpolation over Q^2 are compared with the results from the $\pi^+\pi^- p$ data. Right: $N(1520)3/2^-$ electrocouplings from the πN and $\pi^+\pi^- p$ data for $Q^2 = 0.25$–5.0 GeV^2. The results from πN electroproduction [10] are shown by the red circles. The electrocouplings from the $\pi^+\pi^- p$ differential cross sections measured with CLAS for $Q^2 = 0.25$–1.5 GeV^2 [11,12] are shown by the green triangles. The electrocouplings determined within the JM23 model are shown by the magenta diamonds. The photocouplings from the PDG [14] and from the CLAS πN photoproduction data [58] are shown by the blue triangles and squares, respectively.

TABLE X. Mass and total/partial decay widths of the $\Delta(1600)3/2^+$ into $\pi\Delta$ determined from the fit of $\pi^+\pi^-p$ electroproduction cross sections carried out independently within two intervals in Q^2 and within three overlapping intervals in W. The PDG parameters are listed in the bottom row.

W interval (GeV)	Q^2 interval (GeV^2)	Mass (GeV)	Γ_{tot} (GeV)	$\Gamma_{\pi\Delta}$ (GeV)	BF$_{\pi\Delta}$ (%)
1.46–1.56	2.0–3.5	1.55 ± 0.014	244 ± 21	154 ± 21	50–78
1.51–1.61	2.0–3.5	1.57 ± 0.018	259 ± 21	169 ± 22	52–81
1.56–1.66	2.0–3.5	1.57 ± 0.042	256 ± 33	166 ± 34	46–90
1.46–1.56	3.0–5.0	1.56 ± 0.030	249 ± 37	158 ± 37	42–92
1.51–1.61	3.0–5.0	1.56 ± 0.030	249 ± 34	158 ± 34	44–89
1.56–1.66	3.0–5.0	1.58 ± 0.039	263 ± 29	172 ± 29	49–86
PDG	PDG	1.50–1.64	200–300	172 ± 29	73-83

analyses of the πN and $\pi^+\pi^-p$ data were carried out with different Q^2 binnings. For direct comparison, the electrocouplings obtained from πN were interpolated over Q^2, so that the electrocouplings could be compared at the same Q^2 values. The comparison between all currently available electrocouplings for the $N(1440)1/2^+$ and $N(1520)3/2^-$ from CLAS πN and $\pi^+\pi^-p$ electroproduction is shown in Figs. 10 (right) and 11 (right). Overall, good agreement has been achieved between the electrocouplings of both the $N(1440)1/2^+$ and $N(1520)3/2^-$ determined from independent analyses of the πN and $\pi^+\pi^-p$ data.

The πN and $\pi^+\pi^-p$ electroproduction channels account for the largest part of the total meson electroproduction cross sections in the resonance region for $W < 2$ GeV. Their nonresonant amplitudes are different, however, the N^* electrocouplings obtained from independent studies of these channels should be the same at each Q^2, since the resonance electroexcitation and hadronic decay amplitudes into the different final states should be independent. Hence, consistent results on the electrocouplings of the $N(1440)1/2^+$ and $N(1520)3/2^-$ deduced from πN and $\pi^+\pi^-p$ observed within a broad range of Q^2 from the photon point to 5.0 GeV^2 validates the extraction of the $\gamma_v pN^*$ electrocouplings from the $\pi^+\pi^-p$ electroproduction data.

B. Parameters for the $\Delta(1600)3/2^+$

After the discovery of several new excited states of the proton from global multichannel analysis of exclusive meson photo- and hadroproduction data [6], the status of the $\Delta(1600)3/2^+$ was elevated to a four-star firmly established state [14]. This resonance decays preferentially into $\pi\Delta$ and has been included in the JM23 model.

The electrocouplings, mass, and total/partial hadronic decay widths of the $\Delta(1600)3/2^+$ have been determined for the first time from independent analysis of the $\pi^+\pi^-p$ differential cross sections within three overlapping W intervals, 1.46–1.56, 1.51–1.61, and 1.56–1.66 GeV, for $Q^2 = 2.0$–3.5 and 3.0–5.0 GeV^2. The $\Delta(1600)3/2^+$ contributes substantially to each of these intervals.

The mass and hadronic decay parameters of the $\Delta(1600)3/2^+$ determined from independent fits within six overlapping (W, Q^2) bins listed in Table X are consistent within their uncertainties. They are also in good agreement

with reported PDG values [14]. The masses and hadronic decay widths of N^*'s excited in the s channel for $\gamma_v p$ interactions should be Q^2 independent, since the resonance electroexcitation and hadronic decay amplitudes are independent. The resonance hadronic decay widths obtained from the data fit within the three W intervals should also be the same since the corresponding hadronic decay amplitudes are defined at the resonant point $W = M_{N^*}$. Therefore, the results in Table X provide evidence for the manifestation of the $\Delta(1600)3/2^+$ as an s-channel resonance seen in $\pi^+\pi^-p$ electroproduction. Furthermore, the pronounced Q^2 evolution observed in the nonresonant contributions makes interpretation of the $\Delta(1600)3/2^+$ as a singularity of the nonresonant amplitudes or a dynamically generated resonance unlikely. The successful description of the $\pi^+\pi^-p$ electroproduction data within the (W, Q^2) bins listed in Table X achieved with W- and Q^2-independent $\Delta(1600)3/2^+$ mass and total/partial hadronic decay widths has also demonstrated the capability of the JM23 model for the evaluation of the resonant contributions from this state.

The procedure for the extraction of the $\Delta(1600)3/2^+$ electrocouplings is similar to that used for the $N(1440)1/2^+$ and $N(1520)3/2^-$ described in Sec. III. As starting values for the $\Delta(1600)3/2^+$ electrocouplings, we explored a $\pm 50\%$ range around the values predicted by CSM [51]. Under this variation, the $\pi^+\pi^-p$ differential cross sections computed within JM23 are spread within a range that overlaps the measured differential cross sections for the dominant part of the CLAS data points [46,47]. The extracted $\Delta(1600)3/2^+$ electrocouplings within each of the three W intervals are shown in Fig. 12 (left). The nonresonant amplitudes in the three W intervals are different; however, the determined $\Delta(1600)3/2^+$ electrocouplings are the same within their uncertainties. This success solidifies the evidence for the extraction of the $\Delta(1600)3/2^+$ electrocouplings. The final results for the $\Delta(1600)3/2^+$ electrocouplings were determined by combining the results obtained from the data fits in the three W intervals using the procedure described in Sec. IV A. They are listed in Table XI and shown in Fig. 12 (right). Currently, the CLAS $\pi^+\pi^-p$ electroproduction cross sections are the only data from which electrocouplings of this state have become available. Extraction of the $\Delta(1600)3/2^+$ electrocouplings from π^0p electroproduction data [60,61] will be the next important step in the exploration of the structure of this state.
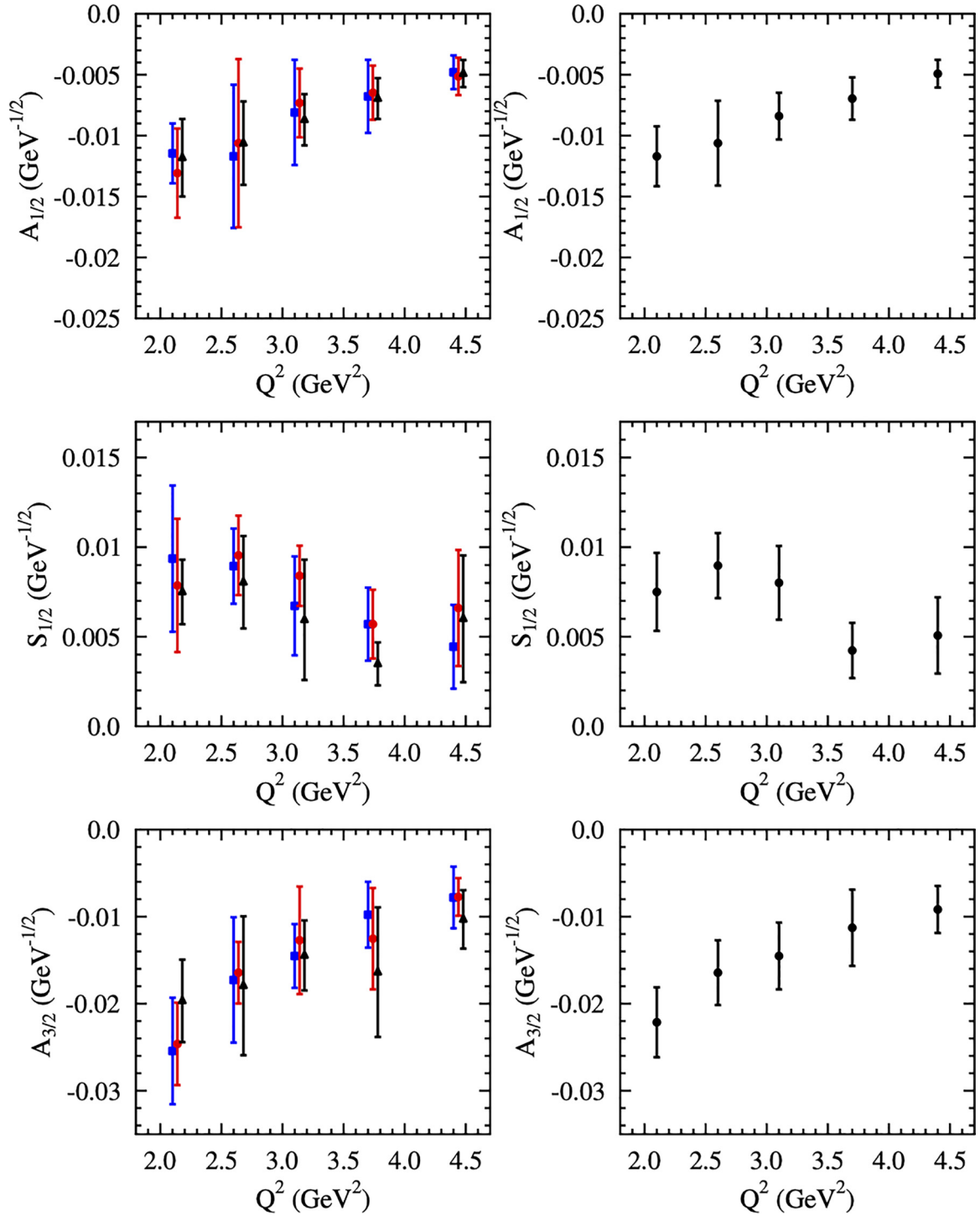
FIG. 12. Left: $\Delta(1600)3/2^+$ electrocouplings deduced from independent fits of the $\pi^+\pi^-p$ differential cross sections carried out within three W intervals, 1.46–1.56 GeV (blue squares), 1.51–1.61 GeV (red circles), and 1.56–1.66 GeV (black triangles), for $Q^2 = 2.0$–5.0 GeV^2. Right: $\Delta(1600)3/2^+$ electrocouplings evaluated by combining the results from the three W intervals as described in Sec. IV A.

V. INSIGHT INTO NUCLEON RESONANCE STRUCTURE

The new results on the $\gamma_v pN^*$ electrocouplings available from the analysis of the CLAS $\pi^+\pi^-p$ electroproduction data for $Q^2 = 2.0$–5.0 GeV^2, together with the previously available results from πN and $\pi^+\pi^-p$ electroproduction off

protons for $Q^2 < 1.5$ GeV^2, provide important input needed to check theory predictions on the structure of N^* states and their emergence from QCD [3,7,8,37]. In this section, we describe new opportunities for the exploration of the structure of the $N(1440)1/2^+$, $N(1520)3/2^-$, and $\Delta(1600)3/2^+$ provided by the results on their electrocouplings.

TABLE XI. $\Delta(1600)3/2^+$ electrocouplings determined from the $\pi^+\pi^- p$ differential cross sections measured with the CLAS detector in three W intervals, 1.46–1.56, 1.51–1.61, and 1.56–1.66 GeV, for $Q^2 = 2.0$–5.0 GeV^2 evaluated as described in Sec. IV A.

Q^2 interval (GeV^2)	$A_{1/2} \times 1000$ (GeV$^{-1/2}$)	$S_{1/2} \times 1000$ (GeV$^{-1/2}$)	$A_{3/2} \times 1000$ (GeV$^{-1/2}$)
2.0–2.4	-11.7 ± 2.5	7.5 ± 2.2	-22.1 ± 4.0
2.4–3.0	-10.6 ± 3.5	9.0 ± 1.8	-16.4 ± 3.7
3.0–3.5	-8.4 ± 1.0	8.0 ± 2.1	-14.5 ± 3.8
3.5–4.2	-7.0 ± 1.7	4.2 ± 1.5	-11.3 ± 4.4
4.2–5.0	-4.9 ± 1.1	5.1 ± 2.1	-9.2 ± 2.7

A. $N(1440)1/2^+$ resonance structure

The CLAS results on the electrocouplings of the $N(1440)1/2^+$ have been described for $Q^2 = 2.0$–5.0 GeV^2 within different approaches. The relativistic light-front quark model [34] and the CSM [43] are shown as representative examples in Fig. 13(a) for the description of its $A_{1/2}$ electrocoupling.

The CSM approach provides a good description in the range of $Q^2 = 2.0$–5.0 GeV^2 of the electrocouplings of the $N(1440)1/2^+$ as a bound quark + diquark system in its first radial excitation [43]. Within this approach, the momentum dependence of the dressed quark and gluon masses has been evaluated from the solution of the QCD equations of motion for the quark and gluon fields. The gluon self-interaction

encoded in the QCD Lagrangian underpins the emergence of the dynamically generated gluon mass, which, at distances on the order of the hadron size, approaches the mass scale of ≈ 0.4 GeV. This process is responsible for the sharp increase of the QCD running coupling α_s/π at distances where perturbative QCD evolves into the strongly coupled QCD (sQCD) regime [39,41]. At quark momenta below 2 GeV, where α_s/π increases rapidly and becomes comparable with unity, the energy stored in the gluon field is transformed into the momentum dependence of the dynamically generated dressed quark mass, which increases rapidly with increasing distance (or inverse quark momentum) and approaches the mass scale of ≈ 0.4 GeV at quark momenta < 0.5 GeV. The dressed quarks with momentum-dependent masses deduced from QCD are treated as the building blocks for the quark core of the ground and excited state nucleons. Their masses and wave functions are obtained from the solution of the Faddeev equations for three dressed quarks in the approximation of a quark + diquark kernel [37,42,43].

The diquark correlations employed in CSM are different in comparison with the rigid diquarks of constituent quark models. In the CSM approach, diquarks represent correlated quark pairs, whose correlation amplitudes are computed as the solution of the Bethe-Salpeter equation with the kernel for the two-dressed-quark interaction mediated by dressed gluon exchange starting from the QCD Lagrangian. The CSM diquark is a dynamical object that interacts with the corresponding third quark, forming a new correlated diquark pair, as shown
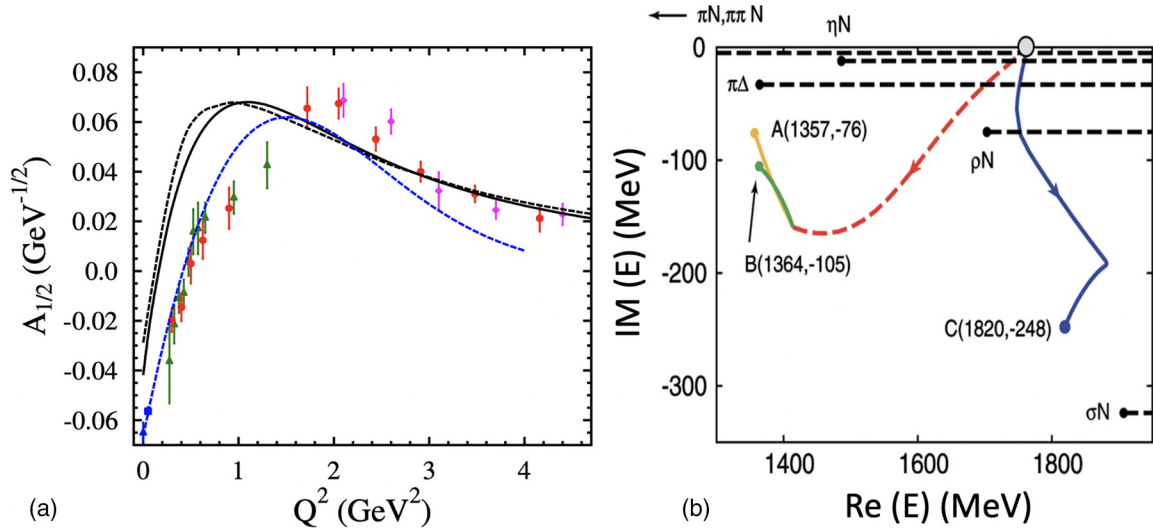

FIG. 13. (a) $N(1440)1/2^+$ $A_{1/2}$ electrocouplings determined from studies of πN electroproduction (red circles) [10] and from $\pi^+\pi^- p$ electroproduction for $Q^2 < 1.5$ GeV^2 (green triangles) [11,12] and for $Q^2 = 2.0$–5.0 GeV^2 available from this work (magenta diamonds). The electrocoupling description within CSM [43], employing a momentum-dependent dressed quark mass deduced from the QCD Lagrangian, is shown by the black solid line. The descriptions achieved within light-front quark models are shown that (i) implement a phenomenological momentum-dependent dressed quark mass [34] (black dashed line) and (ii) account for both an inner core of three constituent quarks and an external meson-baryon cloud [62] (blue dashed line). (b) The evolution of the $N(1440)1/2^+$ complex pole position available from the analysis of meson photo- and hadroproduction data within the Argonne-Osaka coupled-channels approach [7,63] for running values of the meson-baryon couplings from zero (corresponding to the bare quark-core mass on the real energy axis shown by the shaded gray circle) to the finite values determined from the data. The mass of the observed $N(1440)1/2^+$ is determined by the two poles in the complex energy plane labeled on the graph as A and B. The colored lines show the pole movement and splitting as the meson-baryon couplings increase. The horizontal dashed lines show the cuts owing to the opening of the quasi-two-body channels with unstable hadrons.
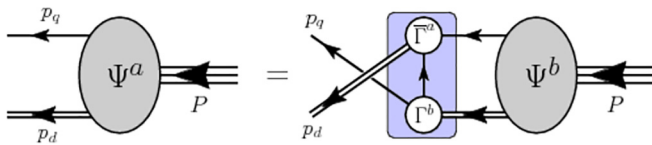
FIG. 14. Faddeev equation for computation of the masses and wave functions of the quark core of the ground and excited states of the nucleon. The kernel for the matrix-valued integral equations is represented by the blue area.

in Fig. 14. The masses of the ground and excited states of the nucleon of a given spin-parity J^P have been obtained as poles in the respective J^P partial waves of the Faddeev amplitude of the three dressed quarks from the solution of the Faddeev equations depicted in Fig. 14. The wave functions for the ground and excited states of the nucleon were obtained from the Faddeev amplitude residues at the pole positions. The electrocouplings are evaluated considering the virtual photon interaction with the electromagnetic currents of the dressed quark and diquark system for the transitions between diquarks of the same or different spin-parities, and account for the virtual photon interaction at the vertex describing diquark decay to or recombination from the pair of uncorrelated quarks shown by the blue shadowed area in Fig. 14 [42].

Within the light-front quark model [34,64], the $N(1440)1/2^+$ is treated as a bound system of three constituent quarks in their first radial excitation. The momentum dependence of the constituent quark mass has been employed in order to reproduce the experimental results on the nucleon elastic form factors. With the same momentum dependence of the constituent quark mass the model has succeeded in providing a reasonable description of the electrocouplings of all N^* states in the mass range up to 1.6 GeV.

As shown in Fig. 13(a), both CSM and the light-front quark model describe the $N(1440)1/2^+$ electrocouplings for $Q^2 = 2.0$–5.0 GeV^2 by employing a momentum-dependent quark mass with virtually coincident predictions. This success demonstrates strong support for quarks with running mass as active structural components in the ground and excited states of the nucleon at distances where the contributions from the quark core become the largest, which occurs at $Q^2 \gtrsim 2$ GeV^2 for the $N(1440)1/2^+$. However, both the CSM [43] and the light-front quark model of Ref. [34] fail to reproduce the $N(1440)1/2^+$ electrocouplings for $Q^2 < 1$ GeV^2. This failure points to additional contributions to the structure relevant at distances on the order of the baryon size. These contributions arise from the meson-baryon cloud. The light-front quark model of Ref. [62], which takes into account the contributions from both the meson-baryon cloud and the quark core to the structure of the $N(1440)1/2^+$, provides a much better description of the data at low Q^2, while retaining a reasonable description at higher Q^2. This feature explains the success of the models that account for only the meson-baryon degrees of freedom in describing the electrocouplings of the $N(1440)1/2^+$ for $Q^2 < 1$ GeV^2 [65–67].

Taking into account the contributions from the quark core and meson-baryon cloud allowed for the resolution of the long-standing puzzle on the ordering of the masses of the radial and orbital excitations in the N^* spectrum. Most quark models with quark interactions mediated by gluon exchange predict the mass of the first radial excitation of three quarks above the mass of the first orbital excitation. The experimental results, in contrast with these quark model expectations, revealed that the mass of the $N(1440)1/2^+$ (1.440 GeV), a state that represents the first radial excitation of three quarks, is below that of the states belonging to the [70, 1$^-$] SU(6) spin-flavor supermultiplet (1.520 and 1.535 GeV for the lightest states) and thus should be expected as the first orbital excitation of three quarks. Coupled-channels analyses of the meson photo- and hadroproduction data carried out by the Argonne-Osaka group [7,63] [see Fig. 13(b)] revealed that, in the limit of zero meson-baryon coupling corresponding to the contribution from just the bare quark core, the mass of 1.76 GeV of the $N(1440)1/2^+$ radial excitation would be above the masses of the lightest N^* in the [70, 1$^-$] supermultiplet, and hence in agreement with the quark model expectations. As the meson-baryon couplings increase toward the values established in the data analysis, the single pole on the real energy axis moves into the complex energy plane and eventually splits into two poles A and B related to the $N(1440)1/2^+$ properties, while the third pole C moves toward the mass range above 1.7 GeV as shown in Fig. 13(b). Therefore, the meson-baryon dressing is responsible for the shift of the bare quark core mass down to the value of the measured mass, below the lightest states in the [70, 1$^-$] supermultiplet.

The CLAS results on the $N(1440)1/2^+$ electrocouplings available over a broad range of $Q^2 < 5.0$ GeV^2 (see Fig. 13) have revealed its structure as an interplay between the inner core of three dressed quarks in their first radial excitation augmented by the external meson-baryon cloud. The meson-baryon degrees of freedom are most relevant for $Q^2 \lesssim 1$ GeV^2, while photons of virtualities $Q^2 \gtrsim 2$ GeV^2 interact mostly with the quark core. Therefore, higher Q^2 studies are preferential for the exploration of the quark degrees of freedom in the structure of this state. Thus studies of the N^* electrocouplings over a broad Q^2 range are necessary to establish the relevant degrees of freedom in their structure and to shed light on their distance-dependent evolution.

The CSM analysis has provided predictions for the quark core wave function of the $N(1440)1/2^+$ in terms of quark + diquark configurations of certain values of the orbital angular momentum of the quark relative to the diquark, as well as for certain isospin and spin-parity values for the diquarks [68]. The Faddeev equations are Poincaré covariant and their solution is available in any reference frame. For comparison with the quark model expectations, the quark + diquark content in the analysis of Ref. [68] was evaluated in the resonance rest frame.

Evaluations of the contributions from quark + diquark configurations into the resonance mass within CSM showed that the dominant part of the bare quark core mass of the $N(1440)1/2^+$ is created by a configuration with a scalar diquark of spin-parity $J^P = 0^+$ and relative orbital angular momentum $L = 0$ of the quark. This fully relativistic finding based on the QCD Lagrangian is in good agreement with expectations from the majority of constituent quark models [7,21,22,35,64]. However, the evaluation of the contributions

from the quark + diquark configurations in the $N(1440)1/2^+$ wave function has revealed a more complex pattern: (a) the contributions from scalar $J^P = 0^+$ and axial-vector diquarks become comparable and (b) higher orbital angular momenta of the quark also contribute to the wave function. Therefore, studies of only the spectrum of N^* states have limited sensitivity to their structure. Any statement on N^* structure based solely on analysis of the N^* spectrum is tenuous as such studies only account for the wave function behavior at distances comparable with the hadron size. The full complexity of the N^* wave function can be mapped out from the results on the Q^2 evolution of the electrocouplings as they are sensitive to all configurations contributing to the wave function and their distance-dependent evolution.

Lowest-order Chebyshev projections for all configurations contributing to the $N(1440)1/2^+$ quark core wave function evaluated within CSM [68] revealed zeros in their dependencies on the relative quark + diquark momentum. This serves as evidence for a radial excitation in the three quark system. Again, this finding, obtained under direct connection to QCD, explains the success of the quark model results [7,21,22,35,64] for the quark core of the $N(1440)1/2^+$ as a radial excitation of the three quark system. The good description of the $N(1440)1/2^+$ electrocouplings obtained from the $\pi^+\pi^-p$ electroproduction data of this work and from πN electroproduction for $Q^2 = 2.0$–5.0 GeV^2 achieved with CSM supports these predictions on its quark core wave function.

B. $N(1520)3/2^-$ resonance structure

The detailed and consistent information on the electrocouplings of the $N(1520)3/2^-$ available for $Q^2 < 5.0$ GeV^2 from the studies of πN and $\pi^+\pi^-p$ electroproduction sheds light on the relevant degrees of freedom in its structure. From its SU(6) assignment, the quark core of the $N(1520)3/2^-$ can be described as three quarks in the octet flavor SU(3)-multiplet of mixed permutation symmetry with spin $S = 1/2$ and orbital angular momentum $L = 1$ [22,69]. The predicted $N(1520)3/2^-$ electrocouplings accounting for only this three-quark configuration have become available from the relativistic quark model [69] and are shown in Fig. 15 by the dotted red lines. These predictions are in strong disagreement with the experimental results. These significant discrepancies suggest that the structure of the $N(1520)3/2^-$ quark core is more complex than expected from its SU(6) assignment.

A reasonable description of the $N(1520)3/2^-$ electrocouplings has been achieved within the framework of the hypercentral constituent quark model (hCQM) [22]. Within this approach, the space part of the $N(1520)3/2^-$ quark core wave function in the resonance rest frame is described by six coordinates consisting of two solid angles Ω_ρ, Ω_λ, hyperangle ξ, and hyperradius x. Relations between ξ, x, and the ρ and λ vectors that describe the three quark systems can be found in Ref. [22]. Both ξ and x are determined by the coordinates of the three quarks. The wave function of the three-quark system expressed in terms of the hypercentral coordinates effectively accounts for the interactions between the three quarks, resulting in their binding into the quark
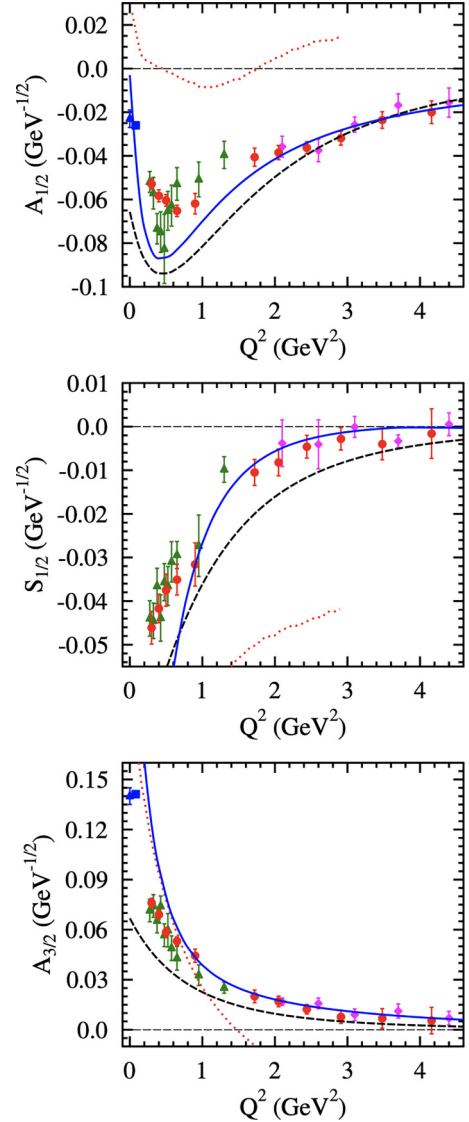

FIG. 15. $N(1520)3/2^-$ electrocouplings determined from studies of πN electroproduction (red circles) [10], and from $\pi^+\pi^-p$ electroproduction for $Q^2 < 1.5$ GeV^2 (green triangles) [11,12] and for $Q^2 = 2.0$–5.0 GeV^2 available from this work (magenta diamonds): $A_{1/2}(Q^2)$ (top), $S_{1/2}(Q^2)$ (middle), and $A_{3/2}(Q^2)$ (bottom). The electrocoupling descriptions achieved within the light-front quark model that includes only the three-quark configuration expected for the SU(6) assignment of the $N(1520)3/2^-$ [69] are shown by the dotted red lines. The results of the light-front quark model [34] that employs three quark configuration mixing and a phenomenological parametrization for the running quark mass and from the hypercentral constituent quark model [22] are shown by the solid blue and dashed black curves, respectively.

core. The confining potential employed in the hCQM is a function of x and consists of two parts: A Coulomb term relevant for distances close to the pQCD regime $\propto 1/x$ and a linear confining part $\propto x$. The SU(6)-violating part of the qq interaction consists of the hyperfine term stemming from vector particle exchange between the two quarks and the quark-flavor mixing term mediated by pseudoscalar meson

exchange. Both terms are supported qualitatively by the CSM approach [25,42]. The dressed gluon exchange represents the vector particle exchange between two quarks, while pseudoscalar meson exchange could be traced back to dynamical chiral symmetry breaking at distances comparable with the baryon size scale. Both SU(6) violating terms and the linear confining term underlie the three-quark configuration mixing. The electrocouplings of most N^*'s have been computed within the hCQM for $Q^2 < 5.0$ GeV^2, keeping all model parameters at the values that fit the N^* spectrum. The hCQM results on the Q^2 evolution of the $N(1520)3/2^-$ electrocouplings [22] are shown in Fig. 15 by the dashed black lines, and a reasonable description has been achieved for $Q^2 > 2.5$ GeV^2.

The $N(1520)3/2^-$ electrocouplings have also been computed within the light-front quark model [34] and are shown in Fig. 15 by the solid blue lines. The major features of this model were highlighted in Sec. V A. The electrocouplings of most N^*'s in the mass range below 1.6 GeV have been evaluated within this model by employing the same momentum-dependent quark mass deduced from the fit of the electromagnetic nucleon elastic form factors. A reasonable description of the CLAS results for the $N(1520)3/2^-$ electrocouplings has been achieved for $Q^2 = 1.5$–5.0 GeV^2. The analysis of the CLAS results on the $N(1440)1/2^+$ and $N(1520)3/2^-$ electrocouplings within the light-front quark model [34] suggests that quarks with momentum-dependent mass represent the active degrees of freedom for the quark core structure of these states. Studies of the $N(1520)3/2^-$ electrocouplings within these models [22,34] have also demonstrated the important role of three-quark configuration mixing in the generation of this state. However, both of these models fail to describe the $N(1520)3/2^-$ electrocouplings for $Q^2 \lesssim 1$ GeV^2. These discrepancies are suggestive of substantial meson-baryon cloud contributions relevant at distances comparable with the baryon size. The CLAS results on the $N(1520)3/2^-$ electrocouplings show that its structure arises as a convolution between the external meson-baryon cloud and the inner core of three dressed quarks.

The contributions from different quark + diquark configurations to the quark core of the $N(1520)3/2^-$ have been evaluated within the CSM approach [70]. These studies demonstrated that 92% of its quark core mass is generated by configurations with axial-vector diquarks of $J^P = 1^+$, while the combined contributions of the configurations with scalar $J^P = 0^+$ and axial-vector diquarks account for almost 100% of the quark core mass, and with respect to the relative angular momentum the P-wave quark in the quark + diquark rest frame generates 98% of the $N(1520)3/2^-$ quark core mass. These CSM evaluations demonstrate that the dominant part of the quark core mass of this state is created by quark + diquark configurations consistent with its SU(6) assignment as the first orbital excitation of three quarks of $L = 1$ and total quark spin $S = 1/2$.

However, analysis of the contributions from quark + diquark configurations to the Faddeev amplitude or wave function of the $N(1520)3/2^-$ reveals a more complex pattern that becomes evident in the studies of the contributions from the pairs of quark + diquark configurations with orbital angular momenta L and L' in the canonical normalization
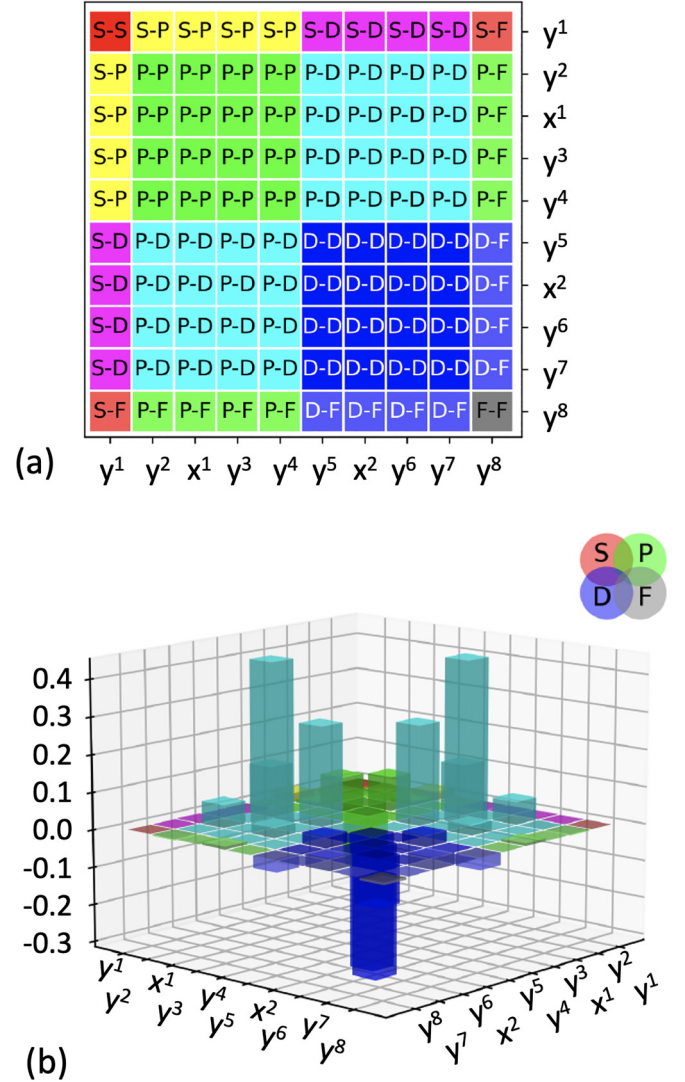

(a)

(b)

FIG. 16. (a) Color map for the contributions to the $N(1520)3/2^-$ wave function from quark + diquark configurations with L and L' orbital angular momenta in the canonical normalization constant of the N^* wave functions accounting for S, P, D, and F quark orbital angular momenta. Here, L and L' represent the quark orbital angular momenta in the resonance wave function and its conjugate, respectively. The axis labels represent the parts of the Faddeev amplitude that contain this information [70]. (b) The contributions from the pairs of quark + diquark configurations to the canonical normalization constant of the $N(1520)3/2^-$ quark core wave function computed within CSM [70] in the resonance rest frame. The color code is shown in panel (a).

constant for the resonance wave function evaluated in its rest frame. Here, L and L' represent the quark orbital angular momenta in the resonance wave function and its conjugate, respectively. The results are shown in Fig. 16. The major part of the $N(1520)3/2^-$ quark core wave function is determined by interference between P and D waves and by the negative contribution of the D wave. The contribution from the P wave is smaller but non-negligible. These results qualitatively support the quark model findings on the substantial role of quark configuration mixing in the $N(1520)3/2^-$

quark core wave function. The CSM studies demonstrated that the spectroscopic $N(1520)3/2^-$ mass is determined by just a P-wave quark + diquark configuration consistent with the SU(6) assignment for this state. Therefore, studies of only the N^* spectrum do not have sufficient sensitivity to elucidate the complexity of its structure. Indeed, the resonance masses are determined by just the long wavelength part of the wave function. Instead, the electrocouplings are sensitive to the contributions from different quark + diquark configurations, shedding light on the full complexity of their structure.

Consequently, a comparison between the predicted CSM results on the Q^2 evolution of the $N(1520)3/2^-$ electrocouplings with the results determined from the πN and $\pi^+\pi^- p$ electroproduction data measured with CLAS provides a sensitive tool for validation of the CSM expectations on the complexity of quark + diquark configuration mixing in the $N(1520)3/2^-$ wave function obtained under a traceable connection to the QCD Lagrangian. The evaluations of the $N(1520)3/2^-$ electrocouplings within CSM are currently in progress.

C. $\Delta(1600)3/2^+$ resonance structure

The predictions of the Q^2-evolution of the $\Delta(1600)3/2^+$ electrocouplings became available in 2019 within the CSM [51]. These evaluations employed the same momentum-dependent dressed quark mass deduced from the QCD Lagrangian and the same framework was used for solving the Faddeev equation to obtain the $\Delta(1600)3/2^+$ wave function as used previously in the description of the $N(1440)1/2^+$ electrocouplings [43]. There are no additional free parameters in the computation of the $\Delta(1600)3/2^+$ electrocouplings. Furthermore, in 2019 no experimental results for the $\Delta(1600)3/2^+$ electrocouplings were available. These have been obtained for the first time from this work. These CSM predictions are shown in Fig. 17 by the solid lines in comparison with the results determined from the data.

The studies of the electrocouplings have demonstrated that the N^* wave functions are determined by the combined contributions from the quark core and meson-baryon cloud. The CSM evaluation of the $\Delta(1600)3/2^+$ electrocouplings accounts for the contribution from only the quark core. Therefore, for comparison with the CSM expectations, the values deduced in this work should be divided by a factor to account for the contribution from only the three quark core component to the full resonance wave function normalization. This factor should be the same for all three $\Delta(1600)3/2^+$ electrocouplings and Q^2 independent. We obtained this factor of 0.6 from the best description of the nine onefold differential cross sections for $W = 1.46$–1.66 GeV and $Q^2 = 2.0$–5.0 GeV^2 by varying the common multiplicative factor for the three $\Delta(1600)3/2^+$ electrocouplings in the range from 0 to 1 with the other parameters of the JM23 model that had been adjusted to fit the $\pi^+\pi^- p$ electroproduction cross section data. Figure 17 shows the electrocouplings from the right column of Fig. 12 divided by a factor of 0.6 and compared with the CSM expectations. The results on the Q^2 evolution of the $\Delta(1600)3/2^+$ electrocouplings deduced from the $\pi^+\pi^- p$
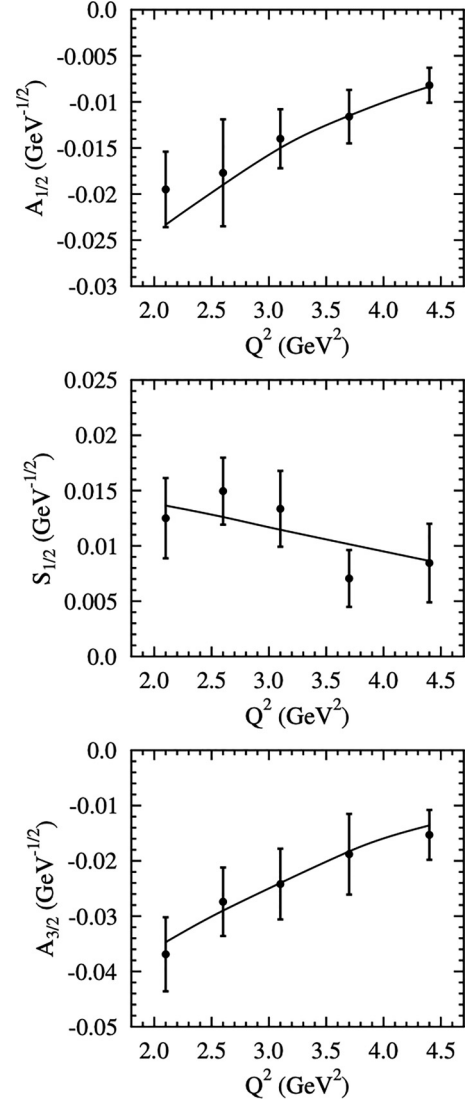

FIG. 17. $\Delta(1600)3/2^+$ electrocouplings obtained in this work: $A_{1/2}$ (top), $S_{1/2}$ (middle), and $A_{3/2}$ (bottom). For comparison with the CSM predictions [51] (solid black lines), the electrocouplings determined from the $\pi^+\pi^- p$ data analysis have been divided by a factor of 0.6 to account for the missing contributions from the meson-baryon cloud in the CSM (see Sec. V C for details).

electroproduction data in this work have confirmed the CSM predictions.

The quark core structure of the $\Delta(1600)3/2^+$ in terms of the contributing quark + diquark configurations has been computed in Ref. [71]. It was found that nearly 100% of the mass of this state is generated by the quark + diquark configuration with an axial-vector diquark of $J^P = 1^+$ and a quark in a relative S wave in the resonance rest frame. The Chebyshev moment of this dominant configuration shows a clear zero crossing, providing evidence for a radial excitation. Hence, the underlying mass generation configuration for the $\Delta(1600)3/2^+$ quark core evaluated within the CSM is consistent with the SU(6) assignment of this state as the first radial excitation of three quarks in an S wave coupled to isospin 3/2.
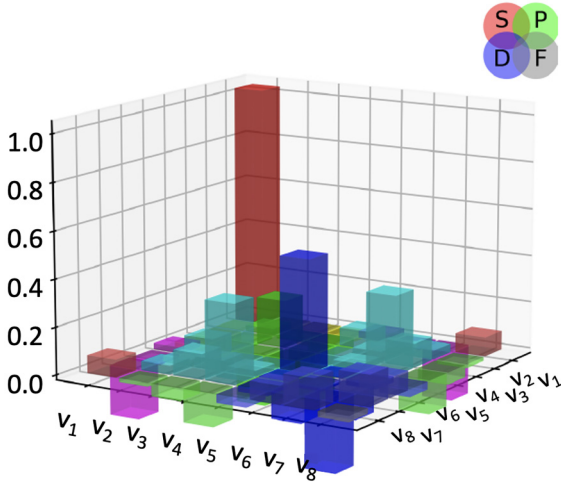
FIG. 18. The contributions of quark + diquark configurations with orbital angular momenta L and L' in the canonical normalization constant of the $\Delta(1600)3/2^+$ quark core wave function computed within CSM in the resonance rest frame [71]. The color code is shown in Fig. 16.

Studies of the contributions of quark + diquark configurations with orbital angular momenta L and L' in the canonical normalization constant for the resonance wave function in its rest frame again revealed a much more complex structure of this state as shown in Fig. 18. The leading contribution arises from interference between S and F waves with subleading contributions from the D wave and interference between P and D waves. As in the case of the $N(1520)3/2^-$, the mass of the $\Delta(1600)3/2^+$ does not have enough sensitivity to unravel the full complexity of the wave function that can only be revealed in the studies of the Q^2 evolution of its electrocouplings. Confirmation of the CSM predictions on the Q^2 evolution of the $\Delta(1600)3/2^+$ electrocouplings by the experimental results obtained in this work validates the structure of its quark core evaluated within CSM under connection to the QCD Lagrangian.

VI. CONCLUSIONS AND OUTLOOK

A good description of the nine independent onefold differential $\pi^+\pi^-p$ electroproduction cross sections off the proton has been achieved within the data-driven JM23 reaction model at $W = 1.41–1.66$ GeV for $Q^2 = 2.0–5.0$ GeV^2. Comparable uncertainties have been achieved for the extracted resonant contributions in the model fits and the measured cross sections. The resonance electrocouplings have been determined from the resonant contributions by employing a unitarized Breit-Wigner ansatz, allowing the restrictions imposed by a general unitarity condition on the resonant amplitudes in exclusive $\pi^+\pi^-p$ electroproduction to be taken into account [11,52]. The $\gamma_v p N^*$ electrocouplings of the $N(1440)1/2^+$, $N(1520)3/2^-$, and $\Delta(1600)3/2^+$ resonances have been determined from the $\pi^+\pi^-p$ electroproduction data for the first time for $Q^2 = 2.0–5.0$ GeV^2.

The electrocouplings of the $N(1440)1/2^+$ and $N(1520)3/2^-$ determined in this work are in good agreement with the results determined independently from the π^+n and

$\pi^0 p$ electroproduction channels [10]. The consistency of the results from independent studies of πN and $\pi^+\pi^-p$ with completely different nonresonant contributions, supports the capabilities of the JM23 reaction model for the extraction of the resonance electrocouplings from $\pi^+\pi^-p$ electroproduction data. Furthermore, consistent results on the electrocouplings of the $N(1440)1/2^+$, $N(1520)3/2^-$, and $\Delta(1600)3/2^+$ for $Q^2 = 2.0–5.0$ GeV^2, available from the independent fits of the $\pi^+\pi^-p$ electroproduction cross sections in three overlapping W intervals with the contribution from the same resonance and different nonresonant amplitudes, solidifies the capability of the JM23 model to provide information on the resonance electrocouplings and their partial hadronic decay widths into the $\pi\Delta$ and ρp final states.

A successful description of the $\pi^+\pi^-p$ electroproduction cross sections achieved for $Q^2 = 0.2–5.0$ GeV^2 [11,12,18] with the same Q^2-independent masses and total/partial hadronic decay widths for the $N(1440)1/2^+$, $N(1520)3/2^-$, and $\Delta(1600)3/2^+$, suggests that these nucleon excited states are produced in the s channel of the $\gamma_v p$ interaction.

The new results on the electrocouplings presented in this work extend the available information on the structure of N^* states in the mass range up to 1.6 GeV. Analyses of these results within the Argonne-Osaka coupled-channels approach [31,32,63], quark models [34,35,62], and within CSM under connection to the QCD Lagrangian [39,43] have revealed the structure of these states as a complex interplay between an inner core of three dressed quarks and an external meson-baryon cloud. Studies of the electrocouplings over a broad range of Q^2 are critical to reveal the structure of these states. At $Q^2 \lesssim 1$ GeV^2, the contribution from the meson-baryon cloud to the interaction with virtual photons at large distances is maximal. With increasing Q^2, photons of high virtuality penetrate the external meson-baryon cloud and interact mostly with the core of three dressed quarks, elucidating the three-quark component in the structure of the N^* states.

Continuum Schwinger methods [38,43] have provided a successful description of the $N(1440)1/2^+$ electrocouplings for $Q^2 = 2.0–5.0$ GeV^2 by employing the momentum dependence of the dressed quark mass deduced from the QCD Lagrangian. The CSM results are virtually the same as those obtained within the relativistic light-front quark model [34,64], which employed a phenomenological momentum-dependent dressed quark mass fit to the results on the nucleon electromagnetic elastic form factors. The predictions of the Q^2 evolution of the $\Delta(1600)3/2^+$ electrocouplings made by CSM in 2019 [51] with the same dressed quark mass function as described above have been confirmed by the results obtained in this work from the $\pi^+\pi^-p$ electroproduction data. All of these studies demonstrate the relevance of dressed quarks with momentum-dependent running mass as the active degrees of freedom in N^* structure.

The results of this work on the electrocouplings of the $N(1520)3/2^-$, as well as the previously available results from the studies of πN electroproduction [10], provide a promising opportunity for CSM and other QCD-based approaches as they become available to explore the relevance of dressed quarks to N^*'s of different structure. In constituent quark

models, this state is treated as three quarks with orbital angular momentum $L = 1$ and belonging to the $[70, 1^-]$ SU(6) spin-flavor multiplet. CSM evaluations of the electrocouplings of this state are currently in progress.

In the near future we are planning to determine from the CLAS $\pi^+\pi^- p$ electroproduction data the electrocouplings of the most prominent nucleon excited states in the mass range of $W = 1.6$–2.0 GeV for $Q^2 = 2.0$–5.0 GeV^2. Analyses of these results provide additional promising opportunities for hadron structure theory to shed light on many facets of the dynamics in the strong QCD regime seen in excited states of the nucleon with different structural features emerge from QCD. These studies also motivate the potential increase of the Jefferson Lab electron beam energy up to 22 GeV, which will offer a unique way to explore the full range of distances where N^* structure emerges in the transition from the perturbative to the strongly coupled QCD regime [72].

[1] V. I. Mokeev and D. S. Carman, Photo- and electrocouplings of nucleon resonances, Few Body Syst. **63**, 59 (2022).

[2] D. S. Carman, K. Joo, and V. I. Mokeev, Strong QCD insights from excited nucleon structure studies with CLAS and CLAS12, Few Body Syst. **61**, 29 (2020).

[3] S. J. Brodsky *et al.*, Strong QCD from hadron structure experiments, Int. J. Mod. Phys. E **29**, 2030006 (2020).

[4] V. I. Mokeev *et al.*, Evidence for the $N'(1720)3/2^+$ nucleon resonance from combined studies of CLAS $\pi^+\pi^- p$ photo- and electroproduction data, Phys. Lett. B **805**, 135457 (2020).

[5] V. I. Mokeev, Two pion photo- and electroproduction with CLAS, EPJ Web Conf. **241**, 03003 (2020).

[6] V. D. Burkert, N^* experiments and what they tell us about strong QCD physics, EPJ Web Conf. **241**, 01004 (2020).

[7] I. G. Aznauryan *et al.*, Studies of nucleon resonance structure in exclusive meson electroproduction, Int. J. Mod. Phys. E **22**, 1330015 (2013).

[8] I. G. Aznauryan and V. D. Burkert, Electroexcitation of nucleon resonances, Prog. Part. Nucl. Phys. **67**, 1 (2012).

[9] K. Park *et al.* (CLAS Collaboration), Measurements of $ep \to e'\pi^+ n$ at $1.6 < W < 2.0$ GeV and extraction of nucleon resonance electrocouplings at CLAS, Phys. Rev. C **91**, 045203 (2015).

[10] I. G. Aznauryan *et al.* (CLAS Collaboration), Electroexcitation of nucleon resonances from CLAS data on single pion electroproduction, Phys. Rev. C **80**, 055203 (2009).

[11] V. I. Mokeev *et al.* (CLAS Collaboration), Experimental study of the $P_{11}(1440)$ and $D_{13}(1520)$ resonances from CLAS data on $ep \to e'\pi^+\pi^- p'$, Phys. Rev. C **86**, 035203 (2012).

[12] V. I. Mokeev, V. D. Burkert, D. S. Carman, L. Elouadrhiri, G. V. Fedotov, E. N. Golovatch, R. W. Gothe, K. Hicks, B. S. Ishkhanov, E. L. Isupov, and I. Skorodumina, New results from the studies of the $N(1440)1/2^+$, $N(1520)3/2^-$, and $\Delta(1620)1/2^-$ resonances in exclusive $ep \to e'p\pi^+\pi^-$ electroproduction with the CLAS detector, Phys. Rev. C **93**, 025206 (2016).

[13] I. G. Aznauryan, V. D. Burkert, G. V. Fedotov, B. S. Ishkhanov, and V. I. Mokeev, Electroexcitation of nucleon resonances at $Q^2 = 0.65$ (GeV/c)^2 from a combined analysis of single- and double-pion electroproduction data, Phys. Rev. C **72**, 045201 (2005).

[14] R. L. Workman *et al.* (Particle Data Group), Review of particle physics, Prog. Theor. Exp. Phys. **2022**, 083C01 (2022).

[15] M. Mai, M. Döring, C. Döring, H. Haberzettl, Ulf-G. Meißner, D. Rönchen, I. Strakovsky, and R. Workman (Jülich-Bonn-Washington Collaboration), Jülich-Bonn-Washington model for pion electroproduction multipoles, Phys. Rev. C **103**, 065204 (2021).

[16] M. Mai, M. Döring, C. Granados, H. Haberzettl, J. Hergenrather, Ulf-G. Meißner, D. Rönchen, I. Strakovsky, and R. Workman (Jülich-Bonn-Washington Collaboration), Coupled-channels analysis of π and η electroproduction within the Jülich-Bonn-Washington model, Phys. Rev. C **106**, 015201 (2022).

[17] H. Kamano, Electromagnetic N^* transition form factors in the ANL-Osaka Dynamical coupled-channels approach, Few Body Syst. **59**, 24 (2018).

[18] V. I. Mokeev, V. D. Burkert, T.-S. H. Lee, L. Elouadrhiri, G. V. Fedotov, and B. S. Ishkhanov, Model analysis of the $p\pi^+\pi^-$ electroproduction reaction on the proton, Phys. Rev. C **80**, 045212 (2009).

[19] B. A. Mecking *et al.*, The CEBAF large acceptance spectrometer (CLAS), Nucl. Instrum. Methods Phys. Res. A **503**, 513 (2003).

[20] R. Koniuk and N. Isgur, Where Have All the Resonances Gone? An Analysis of Baryon Couplings in a Quark Model With Chromodynamics, Phys. Rev. Lett. **44**, 845 (1980).

[21] S. Capstick and W. Roberts, Quark models of baryon masses and decays, Prog. Part. Nucl. Phys. **45**, S241 (2000).

[22] M. M. Giannini and E. Santopinto, The hypercentral constituent quark model and its application to baryon properties, Chin. J. Phys. **53**, P020301 (2015).

[23] E. Klempt and J.-M. Richard, Baryon spectroscopy, Rev. Mod. Phys. **82**, 1095 (2010).

[24] R. G. Edwards, J. J. Dudek, D. G. Richards, and S. J. Wallace, Excited state baryon spectroscopy from lattice QCD, Phys. Rev. D **84**, 074508 (2011).

[25] C. Chen, G. I. Krein, C. D. Roberts, S. M. Schmidt, and J. Segovia, Spectrum and structure of octet and decuplet baryons

and their positive-parity excitations, Phys. Rev. D **100**, 054009 (2019).

[26] M. Ripani *et al.* (CLAS Collaboration), Measurement of $ep \rightarrow e'p\pi^+\pi^-$ and Baryon Resonance Analysis, Phys. Rev. Lett. **91**, 022002 (2003).

[27] E. Golovatch *et al.* (CLAS Collaboration), First results on nucleon resonance photocouplings from the $\gamma p \rightarrow \pi^+\pi^- p$ reaction, Phys. Lett. B **788**, 371 (2019).

[28] A. N. Hiller Blin, V. I. Mokeev, and W. Melnitchouk, Resonant contributions to polarized proton structure functions, Phys. Rev. C **107**, 035202 (2023).

[29] A. N. Hiller Blin, W. Melnitchouk, V. I. Mokeev, V. D. Burkert, V. V. Chesnokov, A. Pilloni, and A. P. Szczepaniak, Resonant contributions to inclusive nucleon structure functions from exclusive meson electroproduction data, Phys. Rev. C **104**, 025201 (2021).

[30] A. N. Hiller Blin *et al.*, Nucleon resonance contributions to unpolarised inclusive electron scattering, Phys. Rev. C **100**, 035201 (2019).

[31] N. Suzuki, T. Sato, and T.-S. H. Lee, Extraction of electromagnetic transition form factors for nucleon resonances within a dynamical coupled-channels model, Phys. Rev. C **82**, 045206 (2010).

[32] V. D. Burkert and C. D. Roberts, Colloquium: Roper resonance: Toward a solution to the fifty year puzzle, Rev. Mod. Phys. **91**, 011003 (2019).

[33] I. G. Aznauryan and V. D. Burkert, Extracting meson-baryon contributions to the electroexcitation of the $N(1675)5/2^-$ nucleon resonance, Phys. Rev. C **92**, 015203 (2015).

[34] I. G. Aznauryan and V. D. Burkert, Electroexcitation of nucleon resonances in a light-front relativistic quark model, Few Body Syst. **59**, 98 (2018).

[35] I. T. Obukhovsky, A. Faessler, D. K. Fedorov, T. Gutsche, and V. E. Lyubovitskij, Transition form factors and helicity amplitudes for electroexcitation of negative and positive parity nucleon resonances in a light-front quark model, Phys. Rev. D **100**, 094013 (2019).

[36] V. E. Lyubovitskij and I. Schmidt, Nucleon resonances with higher spins in soft-wall AdS/QCD, Phys. Rev. D **102**, 094008 (2020).

[37] M. Y. Barabanov *et al.*, Diquark correlations in hadron physics: Origin, impact and evidence, Prog. Part. Nucl. Phys. **116**, 103835 (2021).

[38] D. S. Carman, R. W. Gothe, V. I. Mokeev, and C. D. Roberts, Nucleon resonance electroexcitation amplitudes and emergent hadron mass, Particles **6**, 416 (2023).

[39] C.D. Roberts, On mass and matter, AAPPS Bull. **31**, 6 (2021).

[40] J. Rodríguez-Quintero, D. Binosi, C. Chen, Y. Lu, C. D. Roberts, and J. Segovia, Form factors for the nucleon-to-Roper electromagnetic transition at large Q^2, EPJ Web Conf. **241**, 02009 (2020).

[41] C.D. Roberts, Empirical consequences of emergent mass, Symmetry **12**, 1468 (2020).

[42] J. Segovia, I. C. Cloët, C. D. Roberts, and S. M. Schmidt, Nucleon and Δ elastic and transition form factors, Few Body Syst. **55**, 1185 (2014).

[43] J. Segovia, B. El-Bennich, E. Rojas, I. C. Cloët, C. D. Roberts, S.-S. Xu, and H.-S. Zong, Completing the Picture of the Roper Resonance, Phys. Rev. Lett. **115**, 171801 (2015).

[44] C. D. Roberts, D. G. Richards, T. Horn, and L. Chang, Insights into the emergence of mass from studies of pion and kaon structure, Prog. Part. Nucl. Phys. **120**, 103883 (2021).

[45] T. Horn and C. D. Roberts, The pion: An enigma within the Standard Model, J. Phys. G **43**, 073001 (2016).

[46] E. L. Isupov *et al.* (CLAS Collaboration), Measurements of $ep \rightarrow e'\pi^+\pi^- p'$ cross sections with CLAS at 1.40 GeV $< W <$ 2.0 GeV and 2.0 GeV$^2 < Q^2 <$ 5.0 GeV^2, Phys. Rev. C **96**, 025209 (2017).

[47] A. Trivedi, Measurement of new observables from the $\pi^+\pi^- p$ electroproduction off the proton, Few Body Syst. **60**, 5 (2019).

[48] E. Byckling and K. Kajantie, *Particle Kinematics* (University of Jyvaskyla, Jyvaskyla, Finland, 1971), Chaps. I–IV, X.

[49] G. V. Fedotov *et al.* (CLAS Collaboration), Measurements of the $\gamma_v p \rightarrow p'\pi^+\pi^-$ cross section with the CLAS detector for 0.4 GeV$^2 < Q^2 <$ 1.0 GeV^2 and 1.3 GeV $< W <$ 1.825 GeV, Phys. Rev. C **98**, 025203 (2018).

[50] G. V. Fedotov *et al.* (CLAS Collaboration), Electroproduction of $p\pi^+\pi^-$ off protons at $0.2 < Q^2 < 0.6$ GeV^2 and $1.3 < W <$ 1.57 GeV with CLAS, Phys. Rev. C **79**, 015204 (2009).

[51] Y. Lu, C. Chen, Z.-F. Cui, C. D. Roberts, S. M. Schmidt, J. Segovia, and H. S. Zong, Transition form factors: $\gamma^* + p \rightarrow \Delta(1232), \Delta(1600)$, Phys. Rev. D **100**, 034001 (2019).

[52] I. J. R. Aitchison, K-matrix formalism for overlapping resonances, Nucl. Phys. A **189**, 417 (1972).

[53] H. Kamano, B. Julia-Diaz, T. S. H. Lee, A. Matsuyama, and T. Sato, Dynamical coupled-channels study of $\pi N \rightarrow \pi\pi N$ reactions, Phys. Rev. C **79**, 025206 (2009).

[54] I. J. R. Aitchison and J. J. Brehm, Medium-energy $N\pi\pi$ dynamics. 1, Phys. Rev. D **20**, 1119 (1979).

[55] I. J. R. Aitchison and J. J. Brehm, Unitary analytic isobar model for the reaction nucleon-meson to nucleon-meson-meson, Phys. Rev. D **17**, 3072 (1978).

[56] D. M. Manley, Masses and widths of N and Δ resonances, Phys. Rev. D **51**, 4837 (1995).

[57] D. M. Manley and E. M. Saleski, Multichannel resonance parametrization of πN scattering amplitudes, Phys. Rev. D **45**, 4002 (1992).

[58] M. Dugger *et al.* (CLAS Collaboration), π^+ photoproduction on the proton for photon energies from 0.725 to 2.875 GeV, Phys. Rev. C **79**, 065206 (2009).

[59] I. G. Aznauryan, Multipole amplitudes of pion photoproduction on nucleons up to 2 GeV within dispersion relations and unitary isobar model, Phys. Rev. C **67**, 015209 (2003).

[60] N. Markov *et al.* (CLAS Collaboration), Exclusive $\pi^0 p$ electroproduction off protons in the resonance region at photon virtualities 0.4 GeV$^2 \leqslant Q^2 \leqslant 1$ GeV^2, Phys. Rev. C **101**, 015208 (2020).

[61] E. L. Isupov *et al.* (CLAS Collaboration), Polarized structure function $\sigma_{LT'}$ from $\pi^0 p$ electroproduction data in the resonance region at 0.4 GeV$^2 < Q^2 <$ 1.0 GeV^2, Phys. Rev. C **105**, L022201 (2022).

[62] I. T. Obukhovsky, A. Faessler, D. K. Fedorov, T. Gutsche, and V. E. Lyubovitskij, Electroproduction of the Roper resonance on the proton: The role of the three-quark core and the molecular $N\sigma$ component, Phys. Rev. D **84**, 014004 (2011).

[63] N. Suzuki, B. Julia-Diaz, H. Kamano, T. S. H. Lee, A. Matsuyama, and T. Sato, Disentangling the Dynamical Ori-

gin of P_{11} Nucleon Resonances, Phys. Rev. Lett. **104**, 042302 (2010).

[64] I. G. Aznauryan and V. D. Burkert, Nucleon electromagnetic form factors and electroexcitation of low lying nucleon resonances in a light-front relativistic quark model, Phys. Rev. C **85**, 055202 (2012).

[65] T. Bauer, S. Scherer, and L. Tiator, Electromagnetic transition form factors of the Roper resonance in effective field theory, Phys. Rev. C **90**, 015201 (2014).

[66] O. Krehl, C. Hanhart, S. Krewald, and J. Speth, What is the structure of the Roper resonance? Phys. Rev. C **62**, 025207 (2000).

[67] J. Speth, O. Krehl, S. Krewald, and C. Hanhart, The structure of the Roper resonance, Nucl. Phys. A **680**, 328 (2001).

[68] C. Chen, B. El-Bennich, C. D. Roberts, S. M. Schmidt, J. Segovia, and S. Wan, Structure of the nucleon's low-lying excitations, Phys. Rev. D **97**, 034016 (2018).

[69] S. Capstick and B. D. Keister, Baryon current matrix elements in a light front framework, Phys. Rev. D **51**, 3598 (1995).

[70] L. Liu, C. Chen, and C. D. Roberts, Wave functions of $(I, J^P) = (\frac{1}{2}, \frac{3}{2}^\mp)$ baryons, Phys. Rev. D **107**, 014002 (2023).

[71] L. Liu, C. Chen, Y. Lu, C. D. Roberts, and J. Segovia, Composition of low-lying $J = 3/2^\pm \Delta$-baryons, Phys. Rev. D **105**, 114047 (2022).

[72] A. Accardi *et al.*, Strong interaction physics at the luminosity fironter with 22 GeV electrons at Jefferson Lab, arXiv:2306.09360.